On the relationship between cutting forces and anisotropy features in the milling of LPBF Inconel 718 for near net shape parts

José David Pérez-Ruiz [a], Luis Norberto López de Lacalle [a], Gorka Urbikain [a,*], Octavio Pereira [a], Silvia Martínez [a], Jorge Bris [b]

[a] *University of the Basque Country, Aeronautics Advanced Manufacturing Centre, Spain*
[b] *Universidad del Norte, Colombia*

A B S T R A C T

The versatility and potential applications of additive manufacturing have accelerated the development of additive/subtractive hybrid manufacturing methods. LPBF processes are exceptionally efficient at producing complex-shaped, thin-walled, hollow, or slender parts; however, finishing machining operations are necessary to ensure part assembly and surface quality. Rapid solidification during LPBF processes generates columnar grain structures in alloys. This is associated with crystalline textures and anisotropy, and therefore, mechanical properties are highly dependent on space directions, thus affecting cutting force and its variability.

In this study, theoretical and experimental analyses examined the effects of LPBF parameters on cutting forces and the anisotropy of alloys. Therefore, an oblique cutting Taylor based model was proposed to quantify the crystallographic effects on the shear strength. For this, the tool geometry, tool position, and laser scanning strategy were considered along with the microstructures, crystallographic textures and grain morphologies of two samples with different layer thicknesses (low-volumetric energy density (VED) and high-VED) using scanning electron microscopy and electron backscatter diffraction. Peripheral milling operations had been performed under 54 experimental conditions to evaluate the interactions between the machining parameters along with the layer thickness and the microstructural characteristics of printed alloys. The analysis revealed a significant interaction between the direction of the plane of the shear band and the grain orientation along the main axis. Three milling configurations were evaluated. The effects of the layer thickness on the evolution of the cutting force were elucidated. Additionally, the low-VED sample exhibited higher anisotropy in the cutting force compared to the high-VED one. The anisotropy in the latter corresponds to a high, dense <001> ring-like texture; however, the crystallographic effect is lower in the low-VED sample. A good correlation between the cutting force fluctuation and the predicted Taylor factor was obtained. Lastly, the grain boundary density was acceptably correlated with the level of cutting force for both the printed cases.

1. Introduction

Presently, combining additive and subtractive processes into a hybrid manufacturing method is of scientific and industrial interest [1]. Metallic additive manufacturing (AM) is an effective method for obtaining fully functional components [2,3]. Processes such as laser powder bed fusion(LPBF) provide sufficient flexibility for manufacturing complex morphologies that, in certain cases, cannot be produced by subtractive methods. Therefore, LPBF is of particular interest in manufacturing complex shapes and thin walls, such as ducts for aeronautical engines, vanes, and other power system components. Components produced by metallic AM can be classified as having near-net shapes; therefore, machining requirements are finishing ones. Additionally, the assembly of the posterior printed parts along with other components necessitates a milling operation. Milling such parts frequently involves small chip sizes and highly interrupted machining; therefore, models are essential in predicting the cutting forces to ensure the final surface quality.

The additive/subtractive hybrid manufacturing method requires multidisciplinary efforts ranging from a) design methodologies to b) evaluating the elastic and plastic anisotropic natures of the AM

Nomenclature

$VED\left(\frac{J}{mm^3}\right)$	Volumetric energy density
$P(W)$	Laser power
$t(\mu m)$	Layer thickness
$h(\mu m)$	Hatching space
$V_b\left(\frac{mm}{s}\right)$	Laser speed
$\overrightarrow{G}\left(\frac{°c}{m}\right)$	Thermal gradient
$\xi_1(°)$	Angle between the thermal gradient and preferred grain orientation in the epitaxial direction
$\xi_2(°)$	Angle between the thermal gradient and preferred grain orientation in side branching direction
BD	Building direction
$W(\mu m)$	Melt pool width
$D(\mu m)$	Melt pool depth
$\sigma\left(\frac{N}{m^2}\right)$	Equivalent stress
$\tau_c\left(\frac{N}{m^2}\right)$	Resolved shear stress
R_O	Transformation from the tool reference frame to the workpiece frame
R_Φ	Transformation from the shear band reference frame to the equivalent tool frame
R_z	Transformation from the equivalent tool reference frame to the trochoidal reference frame
R_α	Transformation from the trochoidal reference frame to the workpiece reference frame
$[E]$	Slip systems direction cosines
$[\gamma_i]$	Shears related to a crystal orientation i
ε_c^i	Imposed strain in the crystal
$\phi_c^p(°)$	Predicted shear angle
$d\tau$	Total dislocation shear strain
$\tau_c\left(\frac{N}{m^2}\right)$	Critical resolved shear stress
$d\Omega$	Shear strain in the shear band
M_i	Single crystal Taylor factor
$\overline{M}$	Macroscopic Taylor factor
E_S	Displacement gradient
$\phi_c(°)$	Shear angle
$\beta(°)$	Helix tool angle
$\alpha(°)$	Relative engagement angle
C	Transformation from the shear band reference frame to the crystal reference frame
$a_p(mm)$	Axial cutting depth
$a_e(mm)$	Radial cutting depth
$V_c\left(\frac{m}{min}\right)$	Cutting speed
$f_z\left(\frac{mm}{rev}\right)$	Feed per tooth
$\delta(°)$	Grain tilting angle from the BD
$\sigma_y\left(\frac{N}{m^2}\right)$	Yield stress
$K_y\left(\frac{N}{m^2}m^{0.5}\right)$	Hall–Petch function slope
$d(\mu m)$	Equivalent grain diameter
$\Delta F(\%)$	Increase in the cutting force
$G\{\varphi1^T, \varphi^T, \varphi2^T\}(°)$	Tool Euler angles (Bunge notation)
$g\{\varphi1_i^c, \varphi_i^c, \varphi2_i^c\}(°)$	Crystal Euler angles (Bunge notation)
n	Slip plane
b	Slip direction
$\phi(°)$	Engagement angle
ε_w	Macroscopic effective strain tensor

testpieces. These efforts include fixture design, methodologies for interaction control between the initial and final shapes, overstock requirements and finish machining allowance, surface integrity control [4], CAM utilities [5,6] and the effects of the LPBF parameters, laser scanning strategies, and heat treatment on the mechanical properties and anisotropy [7–11]. These were also reported for LPBF-ed Inconel 718 [12–14]. In this regard, Mang et al. [15] investigated the effects of microstructure and fibre textures on the anisotropy and mechanical properties of LPBF-ed Inconel 718 through a tensile test, which was supported by Schmid's law. Chen et al. [16] evaluated the anisotropic mechanical behaviour of an LPBF-processed Ni-based superalloy K418 printed using two laser scanning strategies. Other researchers studied the microstructural characteristics of LPBF-printed parts with respect to surface quality after machining [17,18]. Bai et al. [15,16] performed a directional independence analysis of the hardness, cutting forces, and surface quality of the printed parts of LPBF-ed 18Ni-300 maraging steel and 6511 martensitic stainless steel. They obtained higher cutting forces in the machined LPBF samples, caused by the grain refining effect, compared to the wrought samples.

Anisotropy and microstructural heterogeneity are commonly regarded as two of the primary drawbacks to be rectified in metal AM processes [19]. Although one solution is typically linked to recrystallisation processes, it cannot be employed, in many cases, on thin-walled parts or complex shapes. In machining, anisotropy significantly impacts the stiffness of the parts (and, therefore, associated with vibrations) and the cutting forces. Thus, understanding the interactions between the LPBF parameters, microstructural-crystallographic characteristics and machining parameters, tool geometry, and tool position is essential for

reducing the variability in the cutting forces and improving the surface quality. In this manner, Ni et al. [20] conducted a micro-hardness-based anisotropy analysis on AM-ed Ti-6Al-4V, considering both the microstructure of alloys and the surface quality. In addition, Bai et al. [21] evaluated the machinability of AM-ed CuCrZr by orthogonal cutting, considering the surface quality, chip morphology, and mechanical properties. The theoretical quantification of the anisotropy effect on the cutting forces was mainly investigated for single-crystal metals [22,23] by orthogonal cutting. For example, Lee et al. [24–26] demonstrated, through Taylor's microplasticity theory, the dependence of cutting forces on the feed direction relative to the crystalline orientation for orthogonal cutting. However, there are few studies regarding the anisotropy effect on the cutting forces for oblique cutting in polycrystalline materials, considering that LPBF materials are also regarded as textured and polycrystalline [27,28]. With this reasoning, Fernandez-Zelaia et al. [29] analysed the crystallographic effect of AM-ed CoCrMo on the average cutting forces in slot milling. They obtained moderate deviations when the feed direction for machining ran parallel to the building direction (BD) in samples with a dominant <001> texture. Hence, Fei [30] performed face milling operations on LPBF-ed nickel alloy 625 pieces, obtaining significant differences in the cutting force levels; the reasons for which were not explained. Regarding AM-ed Inconel 718, Ji et al. [31] explored the influence of the microstructure on the machinability of the parts, either printed or heat-treated. They considered peripheral milling and analysed the surface quality and microstructure using an empirical approach. In contrast to the above-mentioned studies, this one presents the influence of the crystallographic effect and grain morphology (size and orientation) on

the directional cutting force response dependency when oblique cutting was applied to LPBF workpieces, considering tool position and geometry.

This study investigates the effect of the LPBF process parameters on the anisotropy of printed alloys as well as on the cutting forces in the peripheral milling of LPBF-ed Inconel 718. Therefore, the crystallographic and grain morphology effects were studied and quantified. A model based on Taylor's microplasticity theory is proposed for peripheral milling in order to obtain the Taylor factor as a shear strength indicator for the AM parts. AM scanning strategies generate specific patterns in the crystallographic distribution; therefore, the fluctuation in the shear strength along the crystalline distribution can correspond to the laser scanning strategy (LSS). Thus, it is possible to quantify the effect of the LPBF process configuration on the subsequent machining operations. To correlate the effect of the grain morphology on the cutting forces, the grain boundary density was quantified. Therefore, LPBF samples were initially manufactured and their microstructural and crystallographic features were subsequently extracted. Lastly, experimental milling tests were performed. The model exhibited a good correlation between the Taylor factor distribution and the measured cutting forces trend.

2. Interaction between the LPBF parameters and the machining features

Cutting force prediction in the machining of AM parts is challenging owing to the nonlinearities of the LPBF process. However, additive (LPBF process) and subtractive (machining) domains share a mutual interaction with key aspects, a few of which include grain size, grain orientation and crystallographic texture. The numerous variables are summarized in Fig. 1.

2.1. Influence of the LPBF parameters on microstructural and crystallographic characteristics

The microstructure of the LPBF-ed components depends on three main aspects: the solidification mode, LSS and volumetric energy density (VED) (see Fig. 1). Moreover, these features depend on the following specific parameters: the laser power (P), layer thickness (t), hatching space (h) and laser speed (V_b).

The epitaxial growth of crystals is frequently reported in literature [32–34] as the most important phenomenon governing the columnar grain microstructure and causing it to appear in nearly all printed alloys, such as Inconel 718 [35,36]. Several studies on the solidification of metals during LPBF, welding or casting processes agree that the thermal gradient ($\vec{G}$) and solidification rate (V_i) are the most significant factors that govern the columnar grain growth [37,38]. In the case of Inconel, it can be concluded that grains are columnar at essentially any value of the solidification rate for a sufficiently high thermal gradient [39].

Thus, the ratio $\frac{\vec{G}}{V_i}$ defines the solidification mode (columnar, mixed, equiaxed), while $V_i^{-m} G^{-n}$ corresponds to the scale or size of the microstructure [32], where m and n are material constants. The solidification rate (V_i) can be calculated using the laser beam speed (V_b) and the angle (θ) formed between the laser beam speed vector and the vector normal to the isotherms of the liquid–solid interface.

Inconel 718 has an FCC crystal structure [40], which allows columnar grain growth in approximately the thermal gradient direction despite being a polycrystalline material [41,42]. In this manner, Rappaz [43] demonstrated that the grain growth during solidification begins
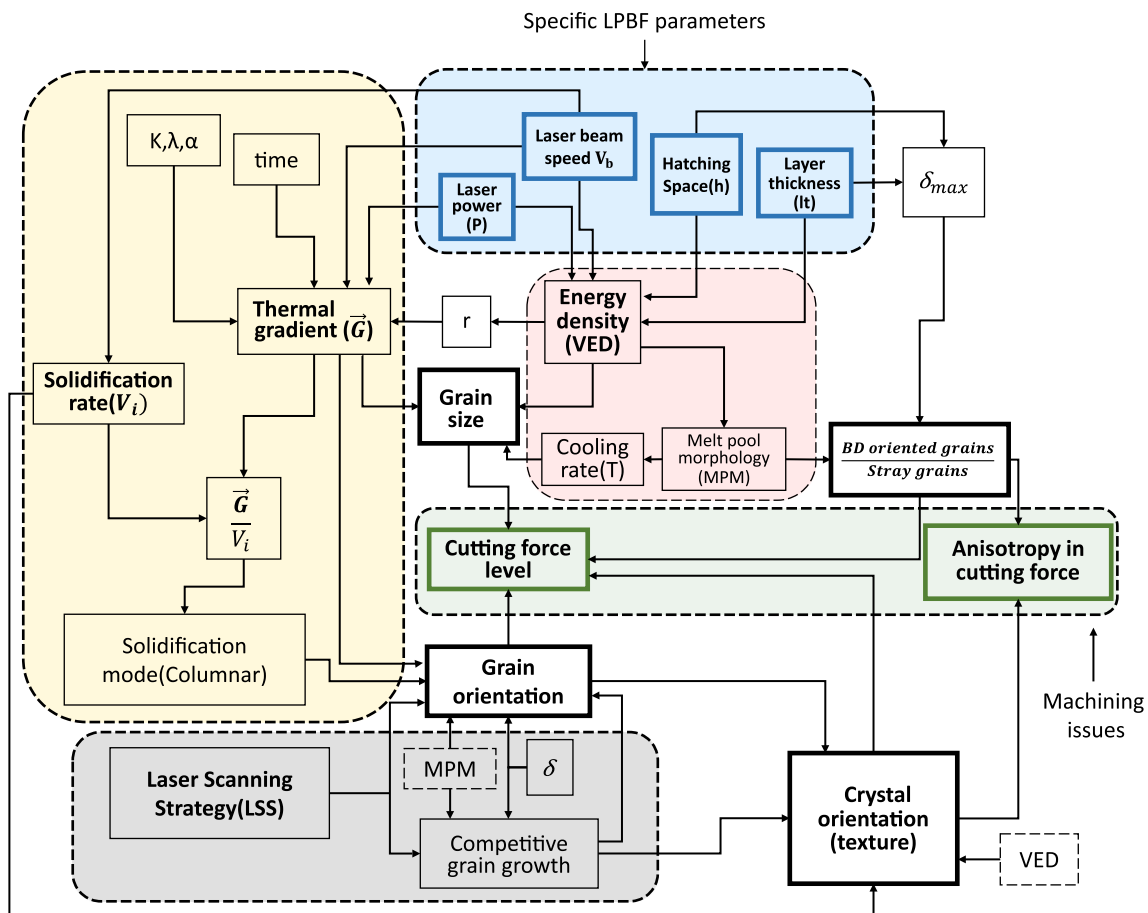

Fig. 1. Interactions between LPBF-microstructure-machining.

with a seed grain (see Fig. 2a) in the unmelted section of the liquid–solid border. The columnar grains formed during the new solidification then begin growing in this seed grain of the substrate, and the growth path approximately follows the direction of the closest thermal gradient G_i [44]. The columnar growth of the grains from the seed grains and the significant influence of the thermal gradient on the direction of their growth are two main factors that allow us to infer the effect of crystallographic texture on the mechanical properties of LPBF-ed components. The literature [33,45] showed that process parameters significantly influence the crystallographic texture of materials printed using LPBF. This phenomenon enables the creation of extended columnar grains that cross multiple layers [16]. The solidification sequence functions quite well when certain scanning strategies (such as unidirectional ones) are applied [38] or in the absence of significant differences between the preferred growth direction and the thermal gradient vector. However, for more complex scanning strategies, the prediction of crystallographic texture is not straightforward. The columnar grain direction depends on multiple factors, among which the thermal gradient, preferred crystallographic direction of the seed grain, competitive grain growth, solidification rate, geometry of the melt pool, and layer thickness are prominent [46,47].

Competitive grain growth frequently occurs in the LPBF process, which implies that the prediction of texture is more complex and closely related to the manufacturing parameters, especially the energy density and laser scanning strategies. The latter and the former play leading roles in determining the texture type [48] and the texture intensity (see Fig. 2b), respectively. An essential aspect of columnar grain growth lies in the role of side branching, which develops when solidification occurs owing to the epitaxial growth of primary dendrites from the secondary ones of previous layers. These originate from the dendrites that grow perpendicular to the epitaxial direction. Angles $\xi1$ and $\xi2$ correspond to the competitive grain growth mechanisms between the thermal gradient and the preferred grain orientation in the epitaxial and the side-branching directions (Fig. 2a, melt pool 1), respectively. Studies conducted by Dinda [38] and Pham [49] showed the significant effect of side branches on crystalline texture development for different scanning strategies, which, in certain cases, produced a texture known as fishbone or chevrons (see Fig. 2b).

The 67-degree scanning direction strategy, wherein the change in the direction of the melt pools shortens the columnar grains, induce a high level of competitive grain growth. However, the grains adopt a zigzag growth pattern to advance along a direction as close as possible to the thermal gradient direction (see Fig. 2a, melt pool 2). The growth of the surrounding dendrites also limits the zigzag growth of the grains. Additionally, the grain spreads across various melt pool boundaries; therefore, the grain size would be reduced for a low energy density (VED) because of the high cooling rates. Likewise, growth through secondary dendrites is limited, and nucleation of disoriented dendrites is possible during the first stage of the solidification of the track (see Fig. 2a – melt pool 3). Afterwards, when the thermal gradient is aligned with a preferred grain crystallographic orientation, columnar grains grow in a direction parallel to the thermal gradient. The disoriented dendrites could correspond to crystalline gradients and dislocations [50].

The effect of the LSS on the texture is shown in Fig. 2b, where the 67-degree rotation strategy is compared with the unidirectional one. When the latter is applied to cubic lattice materials (FCC, BCC), there exist two typical dendritic growth patterns: grain growth in the BD beginning at the bottom of the melt pools and spreading epitaxially through several layers, and oblique grain growth (45°) based on side branching, which occurs sideways with respect to the melt pool. Growth in the BD and oblique grain growth (45°) are associated with the <001 and the <101> textures, respectively. However, the 67-degree rotation strategy is associated with a ring-like <001> texture. In both cases, at higher VED values, the <001> textures tend to be denser [7,51].

The VED is a crucial LPBF parameter that describes the average applied energy per volume of material during powder bed fusion. It involves all the specific LPBF process parameters, such as laser power (P), scanning speed (V_b), hatching space (h) and layer thickness (t) [7]. The VED [52,53] can be calculated using equation (1).

$$VED\left(\frac{J}{mm^3}\right) = \frac{P}{V_b h t} \tag{1}$$

In literature, the effect of VED on grain size has been widely reported [54]. Ng et al. [55] reported that the grain size grew from 2.3 to 4.9 μm when the energy density was increased by using a continuous or pulsed laser. The relationship between VED and grain size passes through two intermediate steps: the melt pool morphology (MPM) and the cooling rate.

The relationship between VED and MPM has been widely reported in literature, establishing a lack of fusion and balling mode for a low VED [56]. However, in the presence of fusion, shallower or steeper melt pool shapes are produced with increasing energy density. However, for an excessive energy density, keyhole-mode melting occurs, and porosities may be produced [56–60] (Fig. 3a). Several studies affirm that the optimal level of energy density to be used in the process agrees with the
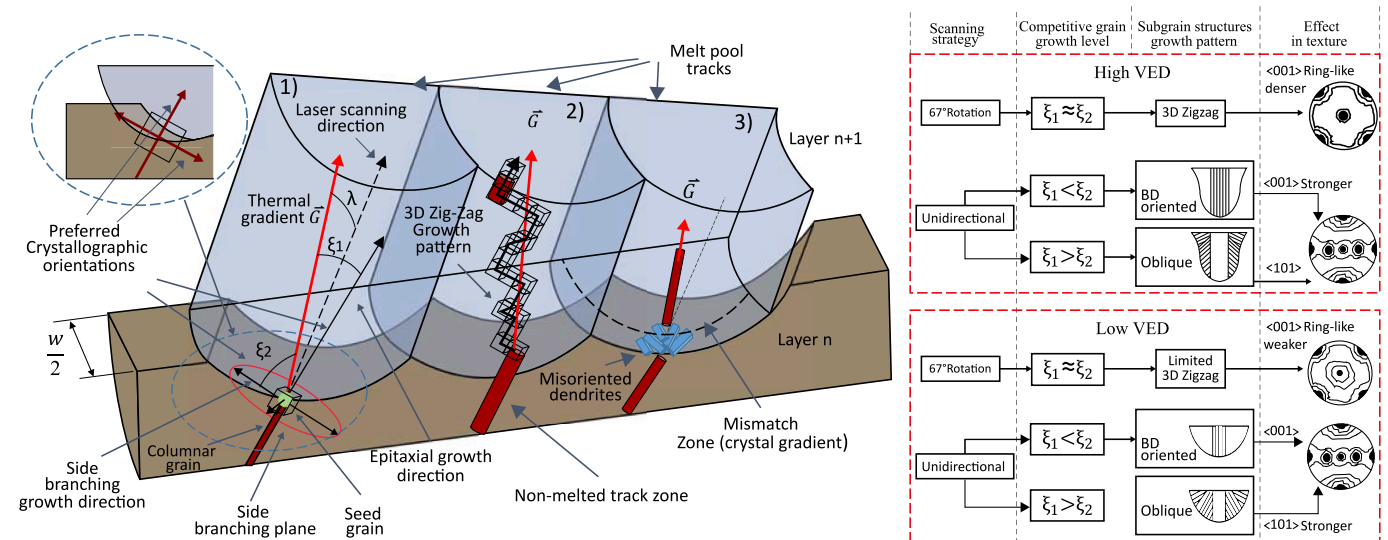

Fig. 2. a). Competitive grain scheme for a 67-degree rotation scanning strategy; b). Effect of scanning strategy and VED on texture.
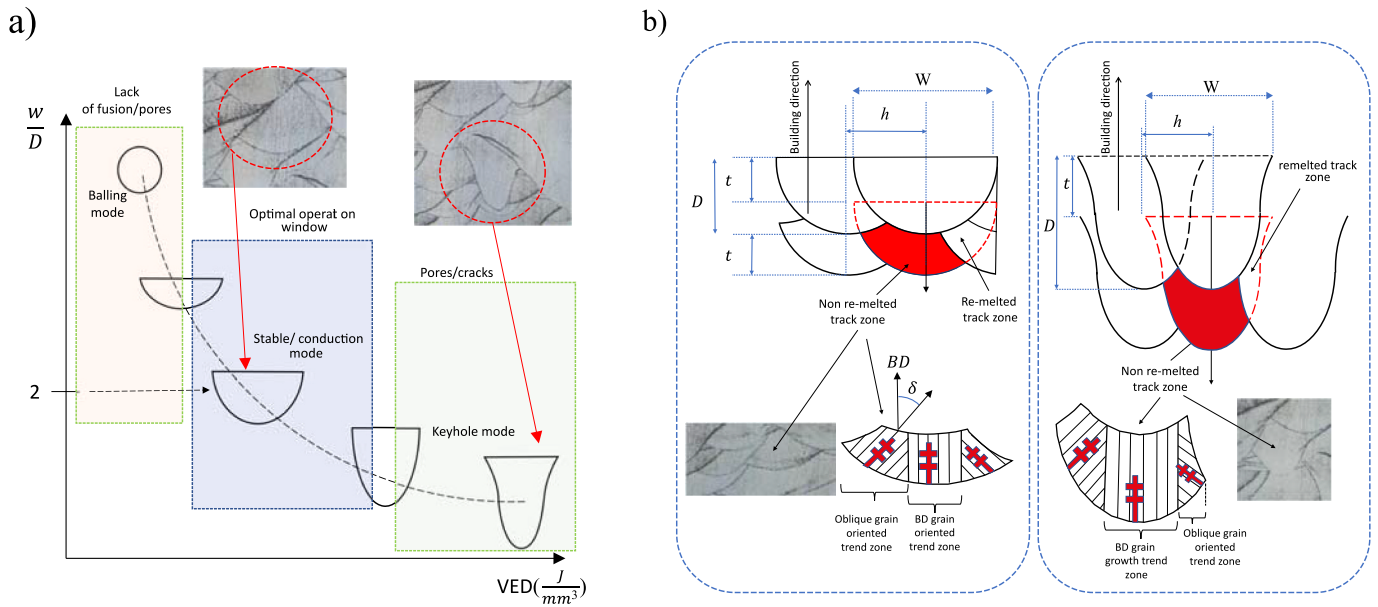
Fig. 3. a) Effect of VED on the melt pool morphology (MPM); b) Types of grain growth trend zones in a non-melted track zone.

conduction mode, where the melt pool presents a W/D ratio ≈ 2. Here, W is the melt pool width and D is the depth of the track (Fig. 3b). Lee et al. proposed an analytical method to predict the melt pool morphology according to a volumetric model of the types of Gaussian heat sources [61].

The relationship between the MPM and the grain size can be understood from the cooling rate. The classical theory of melting and solidification of metals states that the volume of melted material (MPM) increases with the energy density (VED), decreasing the cooling rate. This reduces the number of particles in the nucleation process; thus, the development of constitutional undercooling is affected and the grain size increases [62–64]. However, the study of the quantification of this relationship in LPBF is ongoing. Therefore, Ma et al. [65] proposed a cubic relationship between the cooling rate and the grain size during LPBF.

The MPM influences the volume of the grains parallel to the BD, corresponding to the volume of the grains with oblique directions ($\delta=45°$ or more). The high thermal gradient at the bottom of steeper melt pools causes increased grain growth in the BD. In contrast, for shallower melt pools, the oblique grain growth is denser. A decrease in the layer thickness (t) and hatching space (h) favours a higher density of grains in the BD to the detriment of stray grains owing to their direct geometric relationship with the unmelted track zone geometry. This effect is more significant in steeper melt pools than in shallower ones.

3. Effect of material anisotropy on cutting forces

To evaluate the effect of material anisotropy on the cutting forces, considering the plastic deformation of the cutting process in the slip mode is essential. At the macroscopic level, the cutting area is usually simplified as a plane. At the microscopic level, however, the shear zone is comprised of multiple slip directions, which form what is usually referred to as the plane of the shear band when combined. However, the macroscopic assessment of the cutting process is insufficient to explain the differences in the cutting forces for different positions of the tool concerning the workpiece, This is because it is necessary to evaluate the resistance to dislocations along the direction of the plane of the shear band. An important difference between LPBF and other manufacturing processes is the abundance of columnar grains. Unlike equiaxial grains, they cannot be simplified through an equivalent diameter (d) as it is

necessary to size them at least by a major (d1) and a minor axis (d2). Additionally, columnar grains are more associated with a predominant crystalline orientation.

To assess the resistance to shear action, it is necessary to consider the resistances offered by the grain boundaries [66,67] and by the grain. The Hall–Petch theory and the Zerilli–Armstrong model [68,69] can explain the increase in yield and flow stresses with decreasing grain size. Based on this, it can be inferred that the increase in the grain boundary density is proportional to that in the cutting forces. To evaluate this effect, an analysis of the grain boundary densities for different configurations is presented in Section 6.2. Regarding the resistance to dislocation within the grain, it is necessary to consider the crystalline structure of the material and the interaction between the direction of the strain tensor and the slip systems. Therefore, a model based on Taylor's microplasticity theory was developed in order to evaluate the resistance to dislocation by crystal orientation (Section 3.1).

3.1. Oblique cutting shear strength prediction model

The proposed model is focused on textured polycrystalline materials, and it is based on the work of Lee et al. on single crystals [24]. This model allows the quantification of the shear strength due to the crystallographic effect in any shear plane. This is the result of oblique cutting by end milling through transforming the macroscopic strain tensor from the workpiece reference frame to the crystal reference frame in three steps: firstly, the tool orientation is changed to the workpiece reference frame; secondly, the plane of the shear band is changed from the tool reference frame to the workpiece one; and thirdly, the macroscopic strain tensor can be changed to the crystal reference system once it is in the workpiece reference system. The orientation of a tool corresponding to the workpiece reference system can be fully defined using Euler angles with the Bunge notation (ZYZ). This is defined using Equation (2) and is represented in Fig. 4a.

$$G = \left\{ \varphi 1^T, \varphi^T, \varphi 2^T \right\} \tag{2}$$

The rotation matrix spanning the reference system of the tool and that of the material is obtained from the aforementioned Euler angles (see Equation (3)).
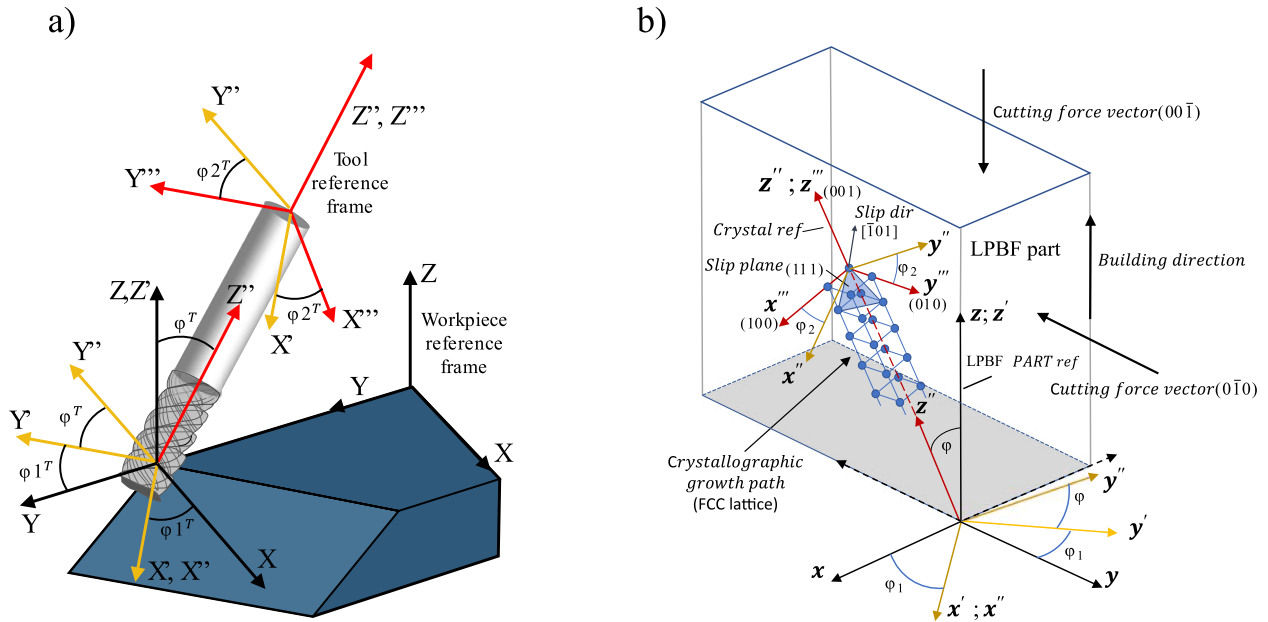
Fig. 4. a) Euler angles in the tool reference frame with respect to the workpiece reference frame; b) Euler angles in the workpiece reference frame with respect to the crystal reference frame.

$$R_O(G) = \begin{bmatrix} \cos(\varphi 1^T)\cos(\varphi^T)\cos(\varphi 2^T) - \sin(\varphi 1^T)\sin(\varphi 2^T) & -\cos(\varphi 1^T)\cos(\varphi^T)\sin(\varphi 2^T) - \sin(\varphi 1^T)\cos(\varphi 2^T) & \cos(\varphi 1^T)\sin(\varphi^T) \\ \sin(\varphi 1^T)\cos(\varphi^T)\cos(\varphi 2^T) + \cos(\varphi 1^T)\sin(\varphi 2^T) & \sin(\varphi 1^T)\cos(\varphi^T)\sin(\varphi 2^T) + \cos(\varphi 1^T)\cos(\varphi 2^T) & \sin(\varphi 1^T)\sin(\varphi^T) \\ -\sin(\varphi^T)\cos(\varphi 2^T) & -\sin(\varphi^T)\sin(\varphi 2^T) & \cos(\varphi^T) \end{bmatrix} \quad (3)$$

Regarding the second step, the plane of the shear band concerning the workpiece reference system is defined by the shear angle ϕ_c, the helix angle β and the relative engagement angle α (see Fig. 5).

$R_{\phi c}$ is the transformation matrix defined by the shear band reference frame (x''', y''', z''') and the equivalent tool reference frame (x'', y'', z'') prescribed by the rotation of ϕ_c. R_Z is the transformation matrix

defined by the equivalent tool reference frame (x'', y'', z'') and the trochoidal position reference frame (x', y', z') prescribed by the rotation of β. Lastly, R_α is the transformation matrix defined by the trochoidal position reference frame (x', y', z') and the workpiece reference frame (x, y, z) prescribed by the rotation of α (see Equation (4) and Fig. 5).
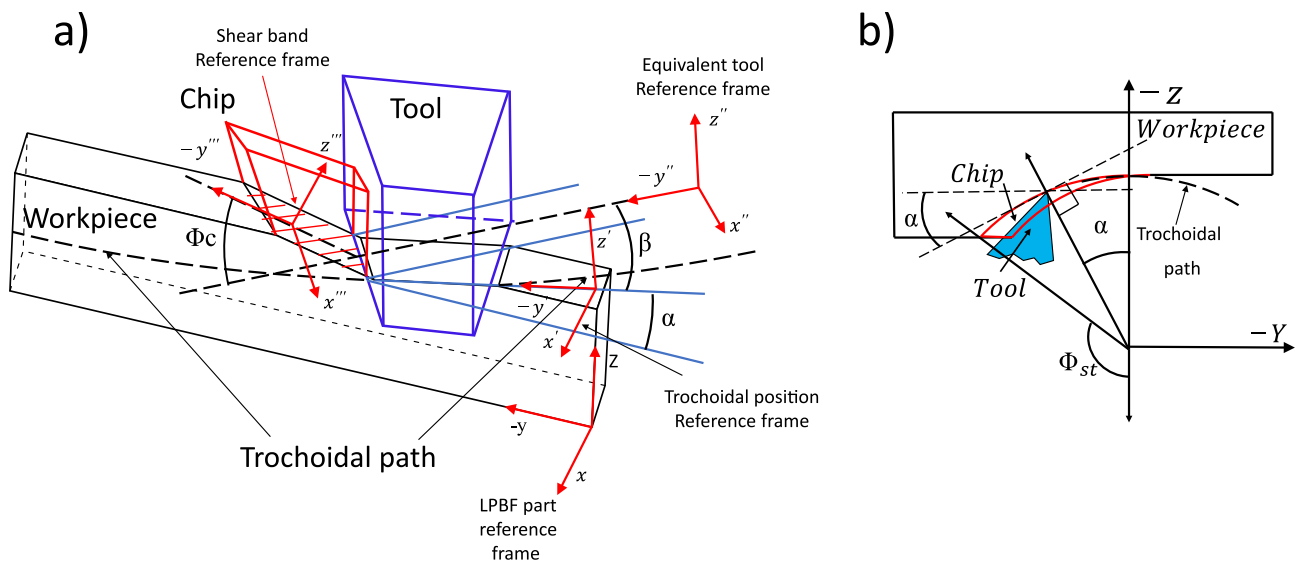

Fig. 5. a) Cutting and shear band geometry; b) Details of engagement by the angle α.

$$R_{\phi c}R_Z R_\alpha = \begin{bmatrix} 1 & 0 & 0 \\ 0 & \cos(\phi_c) & -\sin(\phi_c) \\ 0 & \sin(\phi_c) & \cos(\phi_c) \end{bmatrix} * \begin{bmatrix} \cos(\beta) & \sin(\beta) & 0 \\ -\sin(\beta) & \cos(\beta) & 0 \\ 0 & 0 & 1 \end{bmatrix} * \begin{bmatrix} 1 & 0 & 0 \\ 0 & \cos(\alpha) & \sin(\alpha) \\ 0 & -\sin(\alpha) & \cos(\alpha) \end{bmatrix} \tag{4}$$

The incremental work during a plastic deformation caused by end milling can be defined by

$$dW = \sigma d\varepsilon_w(G, \alpha, \beta, \phi_c), \tag{5}$$

where σ is the equivalent stress and $d\varepsilon_w$ is the macroscopic effective strain tensor in the shear band caused by the cutting process.

The equation for the virtual work done in deforming a single crystal [26] can be written as

$$\sigma d\varepsilon_w = \tau_c \, d\Gamma \; ; \; \frac{\sigma}{\tau_c} = \frac{d\Gamma}{d\varepsilon_w} = M, \tag{6}$$

where $d\Gamma$ is the total dislocation shear strain accumulated in the crystal, σ is the equivalent stress and τ_c is the critical resolved shear stress. M is

$$\varepsilon_w(G, \alpha, \beta, \phi_c) = R_0^T(G)R_\alpha^T R_Z^T R_{\phi c}^T E_S R_{\phi c} R_Z R_\alpha R_0(G), \tag{8}$$

$$E_s = d\Omega/2 \begin{bmatrix} 0 & 0 & 0 \\ 0 & 0 & -1 \\ 0 & -1 & 0 \end{bmatrix}, \tag{9}$$

where E_S is the displacement gradient and $d\Omega$ is the shear strain in the shear band.

The imposed strain in the crystal ε_c^i is obtained using equation (10).

$$\varepsilon_c^i(g_i, G, \alpha, \beta, \phi_c) = C_i(g_i)\varepsilon_w(G, \alpha, \beta, \phi_c)C_i^T(g_i), \tag{10}$$

where C_i is the transformation matrix (Equation (10)) defined by the workpiece reference frame and the crystal reference frame, prescribed by the rotation of $g_i = \{\varphi1_i^c, \varphi_i^c, \varphi2_i^c\}$ (Bunge notation; see Fig. 4b.).

$$C_i(g_i) = \begin{bmatrix} [\cos(\varphi1_i^c)\cos(\varphi_i^c)\cos(\varphi2_i^c) - \sin(\varphi1_i^c)\sin(\varphi2_i^c)] & [-\cos(\varphi1_i^c)\cos(\varphi_i^c)\sin(\varphi2_i^c) - \sin(\varphi1_i^c)\cos(\varphi2_i^c)] & \cos(\varphi1_i^c)\sin(\varphi_i^c) \\ [\sin(\varphi1_i^c)\cos(\varphi_i^c)\cos(\varphi2_i^c) + \cos(\varphi1_i^c)\sin(\varphi2_i^c)] & [\sin(\varphi1_i^c)\cos(\varphi_i^c)\sin(\varphi2_i^c) + \cos(\varphi1_i^c)\cos(\varphi2_i^c)] & \sin(\varphi1_i^c)\sin(\varphi_i^c) \\ -\sin(\varphi_i^c)\cos(\varphi2_i^c) & -\sin(\varphi_i^c)\sin(\varphi2_i^c) & \cos(\varphi_i^c) \end{bmatrix} \tag{11}$$

the Taylor factor, which is the ratio between the microscopic shear strain and the macroscopic strain. Alternatively, it is the ratio between the equivalent normal and shear stresses, implying that higher values of the Taylor factor lead to higher equivalent stresses.

The Taylor factor for oblique cutting in a physically distinctive crystal orientation (g_i) can be defined as

$$M(g_i, G, \alpha, \beta, \phi_c) = \frac{d\Gamma}{d\varepsilon_w(G, \alpha, \beta, \phi_c)} = \frac{\sigma}{\tau_c} = \frac{dW}{\tau_c\varepsilon_c^i(g_i, G, \alpha, \beta, \phi_c)} \quad i$$
$$= 1, 2 \ldots N \tag{7}$$

where N is the number of crystalline orientations evaluated and ε_c is the

According to Taylor's minimum work principle, five independent slip systems are required to develop a plastic strain, considering the incompressibility condition of solids. This implies that an optimisation process must be executed to obtain the combination of the five slip systems that minimises the work due to an imposed strain [70].

The shear required to develop a strain by five independent slip systems is given in Equations (12) and (13), with the former being the compact form of the detailed equation in Equation (13).

$$[\varepsilon_c^i] = [E] \, [\gamma_i] \; or \; [\gamma_i] = [E^{-1}] \, [\varepsilon_c^i], \tag{12}$$

$$\begin{pmatrix} \varepsilon_c^i 22 \\ \varepsilon_c^i 33 \\ \varepsilon_c^i 23 \\ \varepsilon_c^i 13 \\ \varepsilon_c^i 12 \end{pmatrix} = \begin{bmatrix} \left(n\frac{1}{2}b\frac{1}{2}\right) & \left(n\frac{2}{2}b\frac{2}{2}\right) & \left(n\frac{3}{2}b\frac{3}{2}\right) & \left(n\frac{4}{2}b\frac{4}{2}\right) & \left(n\frac{5}{2}b\frac{5}{2}\right) \\ \left(n\frac{1}{3}b\frac{1}{3}\right) & \left(n\frac{2}{3}b\frac{2}{3}\right) & \left(n\frac{3}{3}b\frac{3}{3}\right) & \left(n\frac{4}{3}b\frac{4}{3}\right) & \left(n\frac{5}{3}b\frac{5}{3}\right) \\ \left(n\frac{1}{2}b\frac{1}{3}+n\frac{1}{3}b\frac{1}{2}\right) & \left(n\frac{2}{2}b\frac{2}{3}+n\frac{2}{3}b\frac{2}{2}\right) & \left(n\frac{3}{2}b\frac{3}{3}+n\frac{3}{3}b\frac{3}{2}\right) & \left(n\frac{1}{2}b\frac{1}{2}+n\frac{1}{2}b\frac{1}{2}\right) & \left(n\frac{1}{2}b\frac{1}{2}+n\frac{1}{2}b\frac{1}{2}\right) \\ \left(n\frac{1}{1}b\frac{1}{3}+n\frac{1}{3}b\frac{1}{1}\right) & \left(n\frac{2}{1}b\frac{2}{3}+n\frac{2}{3}b\frac{2}{1}\right) & \left(n\frac{3}{1}b\frac{3}{3}+n\frac{3}{3}b\frac{3}{1}\right) & \left(n\frac{1}{2}b\frac{1}{2}+n\frac{1}{2}b\frac{1}{2}\right) & \left(n\frac{1}{2}b\frac{1}{2}+n\frac{1}{2}b\frac{1}{2}\right) \\ \left(n\frac{1}{1}b\frac{1}{2}+n\frac{1}{2}b\frac{1}{1}\right) & \left(n\frac{2}{1}b\frac{2}{2}+n\frac{2}{2}b\frac{2}{1}\right) & \left(n\frac{3}{1}b\frac{3}{2}+n\frac{3}{2}b\frac{3}{1}\right) & \left(n\frac{4}{1}b\frac{4}{2}+n\frac{4}{2}b\frac{4}{1}\right) & \left(n\frac{5}{1}b\frac{5}{2}+n\frac{5}{2}b\frac{5}{1}\right) \end{bmatrix} \begin{pmatrix} \gamma1_i \\ \gamma2_i \\ \gamma3_i \\ \gamma4_i \\ \gamma5_i \end{pmatrix}, \tag{13}$$

imposed strain in the crystal.

Equation (8) is the expression proposed to obtain the strain tensor in the shear band for oblique cutting during end milling for any tool position in the workpiece reference frame.

where $[E]$ is the direction cosine of any combination of the five slip systems, $[\gamma_i]$ is the corresponding shear related to the crystal orientation

Table 1

Slip systems for the FCC lattice in the crystal reference frame.

Slip plane(n)	(111)			($\bar{1}\bar{1}1$)			($\bar{1}11$)			($1\bar{1}1$)		
Slip direction(b)	[$01\bar{1}$]	[$\bar{1}01$]	[$1\bar{1}0$]	[$01\bar{1}$]	[101]	[$\bar{1}10$]	[$01\bar{1}$]	[101]	[$\bar{1}\bar{1}0$]	[$0\bar{1}1$]	[$\bar{1}01$]	[110]
Slip system	1	2	3	4	5	6	7	8	9	10	11	12

Table 2

Discretization of the crystalline orientation distribution from experimental texture pole figures.

Patterns reported in literature	Laser scanning strategy reported in literature [48]	Crystallographic texture pole figure (PDF) reported in literature [48]	Discrete crystalline orientation distribution (DODF) extracted from the texture pole figure reported in literature (Bunge notation)	Simulated texture plot figure from the DODF
[45,48,73, 74]	Rot-scan	(l)		
[48,74–76]	XY-scan	(k)	<0 0 0>	
[48,74]	X-scan	(j)	<0 0 0> + <0 45 0>	

i, n is the slip plane, b is the slip direction and the superscript corresponds to the slip system. Table 1 lists the slip systems for the FCC lattice.

Once the optimisation process is complete and the five-slip system set is defined, the increment in the plastic work (dW) can be obtained (Equation (13)) and the Taylor factor for oblique cutting in a physically distinctive crystal orientation (g_i) is calculated (Equation (6)). The macroscopic or sample Taylor factor for any combination of G, α, β and ϕ_c can be attained from the previously obtained single-crystal Taylor factors (Equation (7)) using the following equation [71].

$$\overline{M(G, \alpha, \beta, \phi_c)} = \int \int \int M(g_i, G, \alpha, \beta, \phi_c) f(g) dg \qquad (14)$$

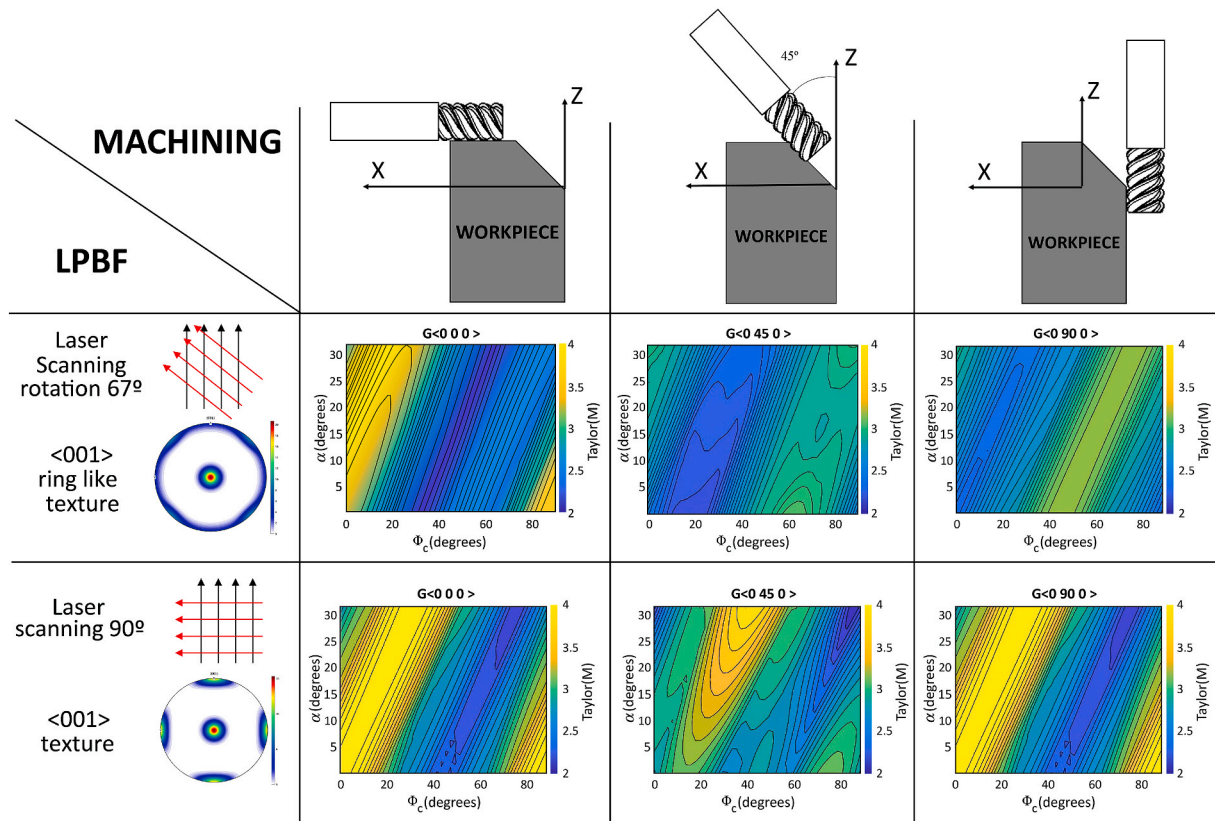Considering that $f(g)$ is the orientation distribution function (ODF;

Fig. 6. LPBF and machining process interaction by ODF patterns.

see Equation (15)),

$$f(g) = ODF(g) = \frac{1}{V}\frac{dV(g)}{dg}, \tag{15}$$

where dV is the volume fraction corresponding to a crystalline direction, dg is the differential of the crystalline orientation and V is the total volume of the Eulerian space (see Equation (16)).

$$V = \int dg = \int d\varphi 1 sin\varphi \; d\varphi 2 = \frac{1}{8\pi^2} \tag{16}$$

The macroscopic (polycrystalline) Taylor factor can then be expressed as a function of the volume fractions using Equation (17).

$$\overline{M(G, \alpha, \beta, \phi_c)} = \int \int \int M(g_i, G, \alpha, \beta, \phi_c)\frac{dV(g)}{V} \tag{17}$$

Obtaining the macroscopic Taylor factor in a shear plane from the crystalline orientations with the highest volume fraction is an approximate but practical solution when machining staff do not possess the experimental information (i.e. EBSD) regarding the crystalline ODF. Considering that laser rotation strategies are evidently associated with the crystalline texture patterns observed in the pole figures, which is widely reported in the literature, it is, therefore, possible to obtain the crystalline orientations with the highest volume fractions from the pole figure of an experimentally obtained crystalline texture (see Table 2). This represents a discretization of the crystalline distribution, which can be a useful approach to analysing the trend of the shear strength of a range of tool positions with respect to the workpiece reference system or when a defined tool orientation and geometry are analysed. The accuracy depends on the number of crystalline orientations considered and the size of the increment in the Euler angles: $g = \{\varphi 1_i^c, \varphi_i^c, \varphi 2_i^c\}$. For rigorous evaluation, using the experimental ODF is recommended.

The volume fraction of a particular orientation can be obtained by multiplying its density by the increment of each Euler angle [72] (see Equation (18)).

$$1 = \frac{1}{8\pi^2}\sum_{\varphi 1}\sum_{\varphi}\sum_{\varphi 2}f(\varphi 1, \varphi_j, \varphi 2)\Delta\varphi 1\Delta\varphi 2\left[\cos\left(\varphi - \frac{\Delta\varphi}{2}\right) - \cos\left(\varphi_j + \frac{\Delta\varphi}{2}\right)\right] \tag{18}$$

Table 2 depicts the use of this technique in the context of LPBF, where discretization of the crystallographic orientation is obtained from the patterns of the pole figures of the textures associated with various laser scanning strategies. The simulated pole figures based on the volumetric fractions and discretized crystalline directions are shown on the right. The patterns of the pole figures reported and the simulated ones are quite similar in the different cases, indicating that the crystalline directions obtained are similar to those of the experimental sample.

From a discrete ODF (DODF) that can be associated with an LSS, the macroscopic (polycrystalline) Taylor factor for any tool orientation can be approximated using Equation (19).

$$\left[\overline{M(G, \alpha, \beta, \phi_c)}\right]^{LSS} \approx \left[\sum_{i=1}^{N}M(G, \alpha, \beta, \phi_c)\frac{dV(g_i)}{V}\right]^{LSS} \tag{19}$$

Owing to the Taylor factor being a good shear strength indicator, the effect of the laser rotation strategy on the shear strength under certain tool positions can be calculated using the proposed model and observed using Taylor maps for different combinations of tool positions (G), shear angles (ϕ_c) relative engagement angles (α), helix angles (β) and laser rotation strategies. Fig. 6 shows six Taylor maps that consider the interaction of two LSSs (rotation by 67° and 90°) with three milling configurations (G(0 0 0), G(0 45 0), G(0 90 0) for $\beta = 30°$, an α range from 0° to 32° and a ϕ_c range from 0° to 90°).

To quantify the material crystallographic effect on the shear strength (or cutting forces) when the cutting tool changed position, it is necessary to determine the variation in the Taylor factor with the tool positions. Therefore, it is necessary to extract a Taylor factor value that represents the shear strength for each tool position. With regards to peripheral milling, there exist different relative engagement angles (α) and shear resistance values associated with each one. The shear angle for each relative engagement angle (α) can be predicted (ϕ_c^p) through the effective Taylor factor M' [24], which is based on the principle of maximum stress. It is calculated as M/cos (2ψ), where ψ is the angle of deviation of the shear angle (ϕ_c) corresponding to an angle of 45°, because the shear strain increases by an order of 1/cos (2ψ) to maintain the macroscopic strain.

Once the shear strength profile (expressed by the Taylor factor) along the tool engagement path is obtained (see Fig. 7), a representative value of the shear strength can be extracted. Considering that the maximum cutting force is usually associated with the maximum chip thickness, which usually occurs in the initial moments of the engagement between the tool and the part, the Taylor factor corresponding to ϕ_{st} can be considered a significant value. Likewise, the mean value can be representative when the variations in the Taylor factor throughout the engagement are not very large.

Fig. 7 shows the variation in the Taylor factor as a function of the engagement angle (α) for down milling for G (0 90 0) and g (45 0 0) with $\beta = 30°$ (see Fig. 24 in the appendix). The white line in Fig. 7b corresponds to the predicted shear angle values (ϕ_c^p) for each α value based on the specific tool position and crystal orientation. Considering that $\phi = 180 - \alpha$, it is then possible to obtain the shear strength profile during engagement using the Taylor factor as a function of the engagement angle (ϕ) (Fig. 7c.).
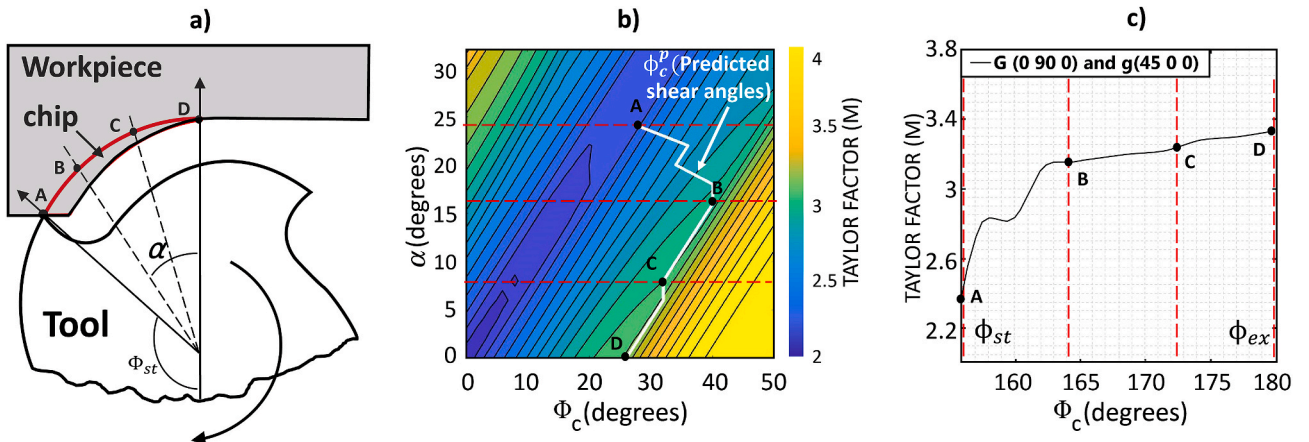

Fig. 7. a) Details of tool engagement; b) Predicted shear angle with respect to the effective Taylor factor; c) Taylor factor in the function of the engagement angle.
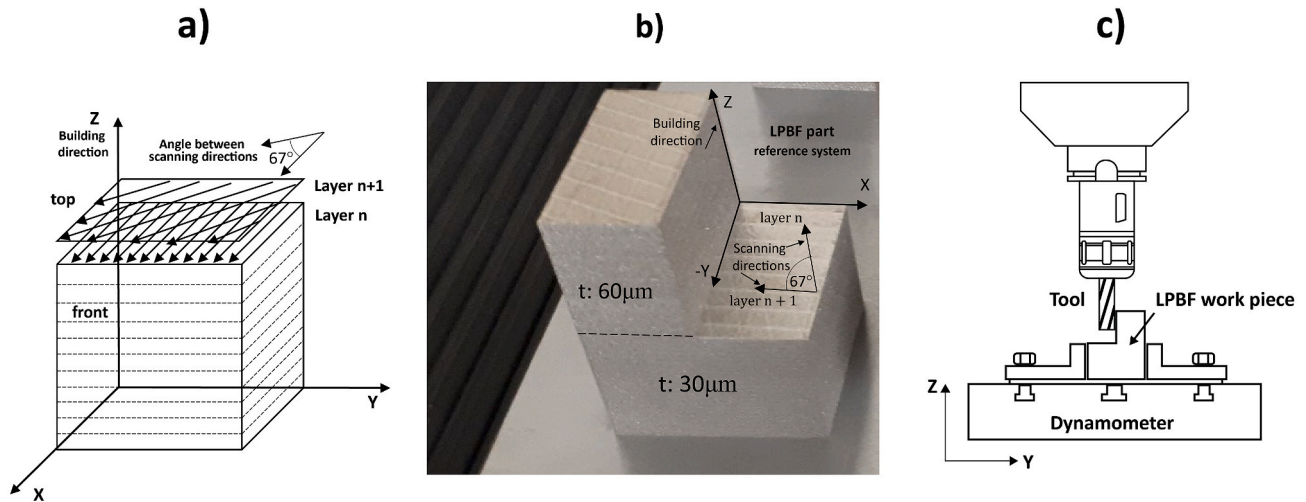
Fig. 8. a) 67-degree rotation scanning direction strategy; b) LPBF-ed Inconel 718 component for characterisation; c) Milling set up.

Table 3
LPBF parameters, cutting parameters, and experimental factors.

LPBF Parameters			Milling experimental factors and levels			
	Zone 1	**Zone 2**	**Factor**	**Low**	**Middle**	**High**
Power (W)	200	200	Feed-f(mm/rev·z)	0.03	0.04	0.05
Speed (mm/s)	1000	1000	a_e (mm)	0.1	0.3	0.5
Hatch spacing (mm)	0.09	0.09	Milling case $(\overrightarrow{a_p}\,\overrightarrow{a_e}\,\overrightarrow{f})$	Case 1 (XZY)	Case 2 (ZXY)	Case 3 (XYZ)
Layer thickness (μm)	30	60	Layer thickness (μm)	30	–	60
Laser beam spot size (μm)	70	70	**Cutting parameters and tool information (HM end mill-4 flutes)**			
			Cutting speed V_c (m/min)	60	Tool diameter (mm)	10
			Axial depth (a_p) (mm)	5	Helix angle β (°)	30

4. Methodology and experimental procedure

Four prismatic samples of Inconel 718 were manufactured simultaneously using a Renishaw AM 400 machine to characterise the cutting forces using end milling. The sample geometry was a 4 × 4 × 8 cm L-cube, as shown in Fig. 8b, having two zones with different layer thicknesses (30 and 60 μm). Layers of 60 μm are used to minimise the processing time, while those of 30 μm are used when precision was required. Layer thicknesses smaller than 30 μm are inconsistent with the feed powder size, and layers larger than 60 μm on Inconel 718 produce excessive internal porosity.

The 30 μm zone (zone 1) was printed first, and the 60 μm zone (zone 2) was added on top. This L-cube shape simplifies machining. A laser rotation strategy of 67°per layer was used (Fig. 8a), which is considered useful for reducing residual stress [77]. The scanning direction was on the XY plane, and the BD was along the Z-axis.

To observe the effect of material anisotropy on oblique cutting forces on LPBF-ed Inconel 718, a factorial experiment design $3^3 2^1$ was adopted. Peripheral milling experiments were performed on a Kondia A6 milling centre with a Fagor 8070 CNC. The milling forces were measured using a Kistler 9255B dynamometer (16384 Hz). Fig. 8c shows a

schematic diagram of the setup used for measuring the cutting force. The tool cutting edge quality was controlled to ensure accuracy of the measurements. A 5 mm axial depth of cut was selected in accordance with the tool diameter; it avoids cutting with the same tooth at two different heights. The selected radial depth of cut range corresponds to the usual stock of material to be removed from a printed piece (in the range of 0.1–0.2 mm). Depending on the orientation of the manufactured parts on the printing plates, these overstocks can be slightly larger. The selected feed range corresponds to one-tenth of the radial depths of cut evaluated, which is in accordance with a superfinishing and low roughness process.

The LPBF parameters, cutting parameters, tool information and experimental factors are listed in Table 3. Additionally, three milling configurations (hereinafter referred to as 'milling cases') were analysed to consider the directional dependence of machinability for LPBF-ed Inconel 718 components; these were the three climb milling types. The end mill tool orientation relative to the LPBF component and the equivalence of the measured cutting forces in the tool and LPBF component reference frames are shown in Fig. 9.

The study of grain features, subgrain structures and crystalline textures was aided by electron microscopic observations using scanning electron microscopy SEM and electron backscatter diffraction (EBSD). Furthermore, the MPM was studied using an optical microscope. Inverse figures, pole figures and Taylor maps were obtained using MTEX. Therefore, two samples of 30 and 60 μm were analysed, as described in the subsequent sections, as lt30 and lt60, respectively. A mapping area of 1000 μm × 1000 μm and a step size of 2 μm were used for EBSD mapping. Additionally, a 12° misorientation angle was used to distinguish different grain boundaries.

5. Results

The results are presented in two steps. Firstly, the effect of LPBF on the microstructure and texture of LPBF-ed Inconel 718 samples is presented in Section 5.1. Secondly, an analyses and characterisations of the cutting force features and machining parameters are presented in Section 5.2.

5.1. Microstructural and crystallographic characterisation

The characterisation of the material was developed in four stages. Firstly, the MPM was evaluated. Secondly, the microstructural characterisation was obtained using EBSD. Thirdly, the grain morphology was characterised. Lastly, the crystallographic textures of the samples evaluated were compared. Hardness was compared using the Rockwell C
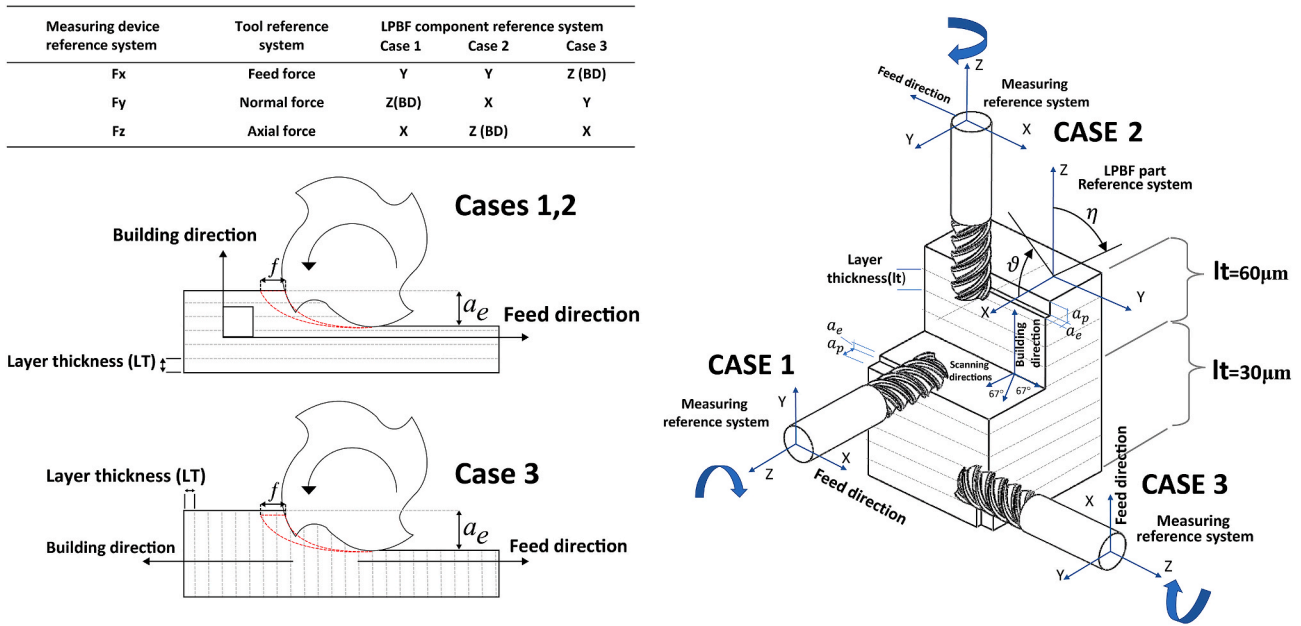
Measuring device reference system	Tool reference system	LPBF component reference system		
		Case 1	Case 2	Case 3
Fx	Feed force	Y	Y	Z (BD)
Fy	Normal force	Z(BD)	X	Y
Fz	Axial force	X	Z (BD)	X

Fig. 9. Conventions for cutting forces in different reference systems by milling cases.
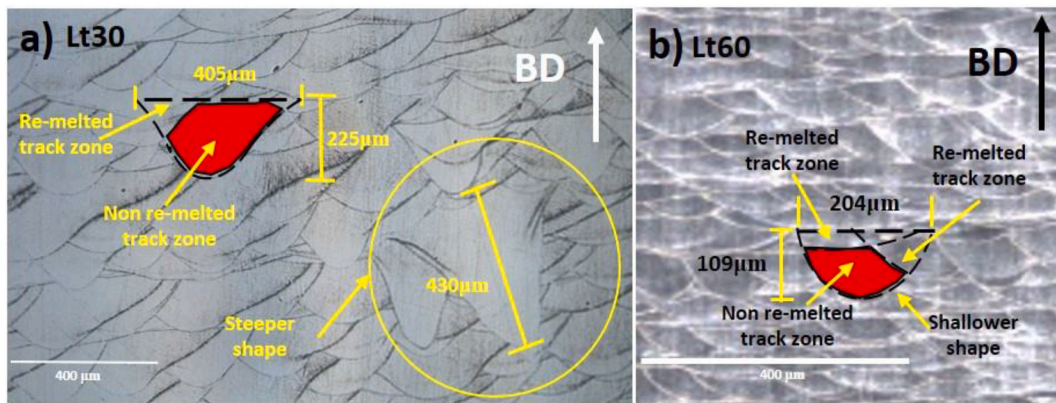

Fig. 10. Melt pool shape characterisation: a) Melt pools corresponding to the lt30 sample; b) Melt pools corresponding to the lt60 sample.

scale for both samples with mean values of 36.4 Rc and 32 Rc for the lt30 and lt60 samples, respectively. This implies that hardness did not appear to be the best criterion to explain the influence of anisotropy on oblique cutting forces for this type of material.

5.1.1. Melt pool shapes and dimensions

The melt pool shapes for the lt30 and lt60 samples are displayed in Fig. 10, with the contours of certain melt pool boundaries outlined for better comprehension. The differences in the shapes and sizes between the melt pools are significant, and the width and depth of the melt pool are observed to be more prominent in the lt30 sample. This is due to a greater VED during the manufacturing process, which produces steeper melt pools in certain cases closer to the keyhole-mode (Fig. 10a). However, the shape of the melt pool was shallower in the lt60 sample (Fig. 10b).

5.1.2. EBSD grain characterisation

EBSD and SEM were performed on the lt30 and lt60 samples. Fig. 11a and g correspond to the YZ planes, while Fig. 11c and j represent the XY planes (upper view) of 30 μm and 60 μm, respectively. Pole figures and inverse pole figures are displayed with <uvw> directions parallel to the BD.

Strong epitaxial growth was observed in both samples in the red <001> and green <011> columnar grains. Notably, a few grains crossed over 20 layers; these grains were frequently localised at the bottom of the melt pools where the thermal gradient is stronger and oriented along the BD. Fig. 11d shows a grain equiaxial arrangement of the lt30 sample, representing the cross-section of the columnar grains (XY plane). This equiaxial arrangement indicates a greater proportion of grains aligned with the BD <001>, represented by the colour red. However, Fig. 11j shows that the grains present rows of small equiaxial grains (reddish) and rows of larger columnar grains with different orientations. The former arise from the bottom of the melt pool tracks and are aligned with the BD, while the latter correspond to the lateral zones of the melt pools having oblique orientations. The high directionality in the lt30 sample is caused by the higher input values of energy densities, leading to lower cooling rates than in the lt60 sample. However, the predominant epitaxial orientation of the grains in the lt30 sample can be corroborated in Fig. 11b and c, which show a predominant epitaxial growth pattern in the columnar dendritic grains. The epitaxial grain growth pattern can also be observed in the cellular structure depicted in Fig. 11f. This is because the grains have a dendritic cellular subgrain structure, which is the cellular structure pattern observed mainly on the XY plane (Fig. 11f) and the dendritic structure pattern observed on the
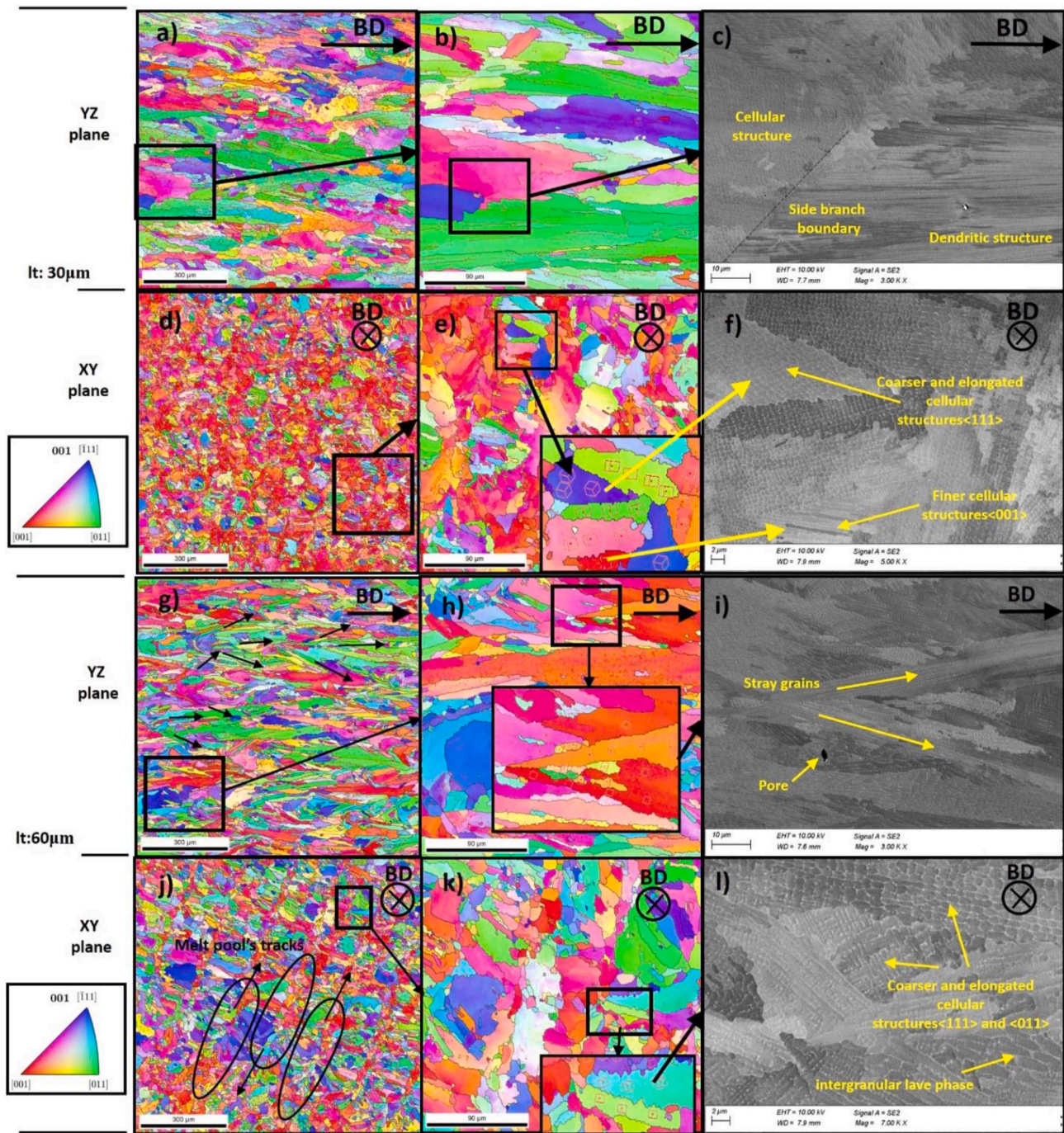
Fig. 11. EBSD and SEM scans of the samples: a) EBSD of lt30 in the YZ plane; b) and c) SEM of lt30 in the YZ plane; d) and e) EBSD of the lt30 sample in the XY plane; f) SEM of the lt30 sample in the XY plane; g) and h) EBSD of lt60 in the YZ plane; i) SEM of lt60 in the YZ plane; j) and k) EBSD of the lt60 sample in the XY plane; l) SEM of the lt60 sample in the XY plane.

YZ plane (Fig. 11c). In Fig. 11c, a few columnar grains in the dendritic epitaxial structure can be observed to be crossing several manufacturing layers, reaching lengths along the BD of over 200 μm, which is equivalent to seven layers or more. This indicates that the strategy of laser rotation at 67°does not prevent epitaxial growth of the grains through the layers at higher energy densities. This behaviour could be explained using the concept of competitive grain growth, which becomes tangible within the observed 3D zigzag grain growth patterns (see Figs. 2b and 12); it is key to understanding how the grains can cross multiple layers despite the 67-degree laser-rotation strategy. The zigzags formed by columnar grains follow the thermal gradient vector, which is the

mechanism used when Inconel 718 crystals grow as close as possible to the thermal gradient direction (see Fig. 2b). The zigzag reflects the alternation between epitaxial and side-branching grain growth along the BD (see Fig. 12).

Fig. 12a and c shows the EBSD maps of the SEM shots displayed in Fig. 12b and d, respectively (lt30 and lt60). In Fig. 12b, zones A, B, C and D represent the sections of grains with dendritic subgrain structures. However, the AA, BB, CC and DD zones represent the sections of the grains with cellular subgrain structures. Notably, A and AA represent sections of the same grain, which can be verified in Fig. 12a, wherein zones A and AA are both in green, which implies that both grain sections
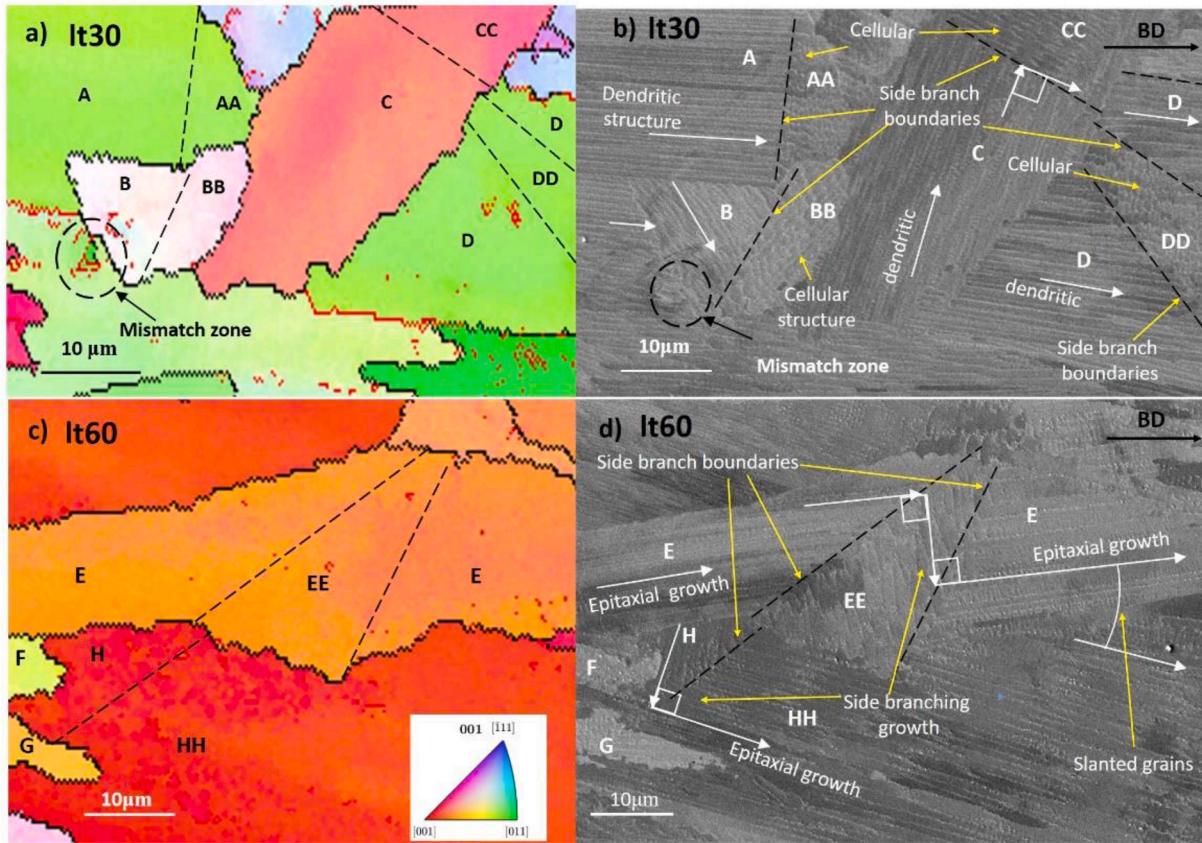
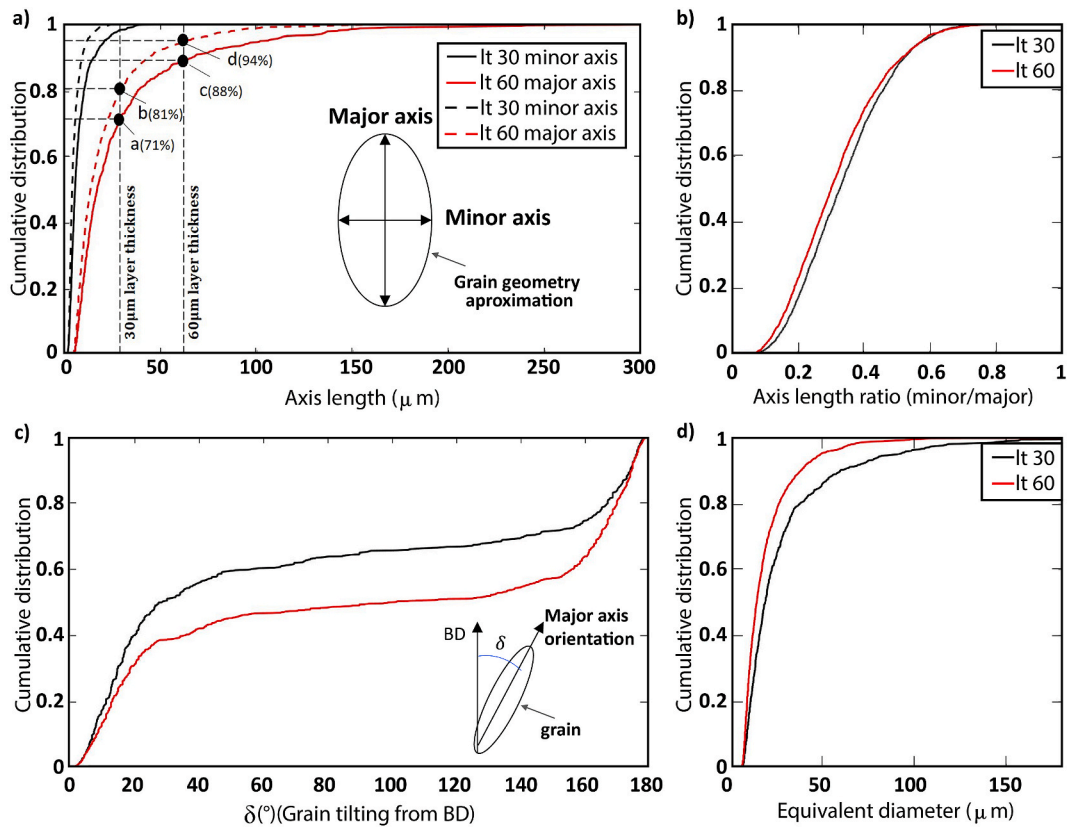**Fig. 12.** 3D zigzag subgrain growth pattern in the lt30 and lt60 samples.
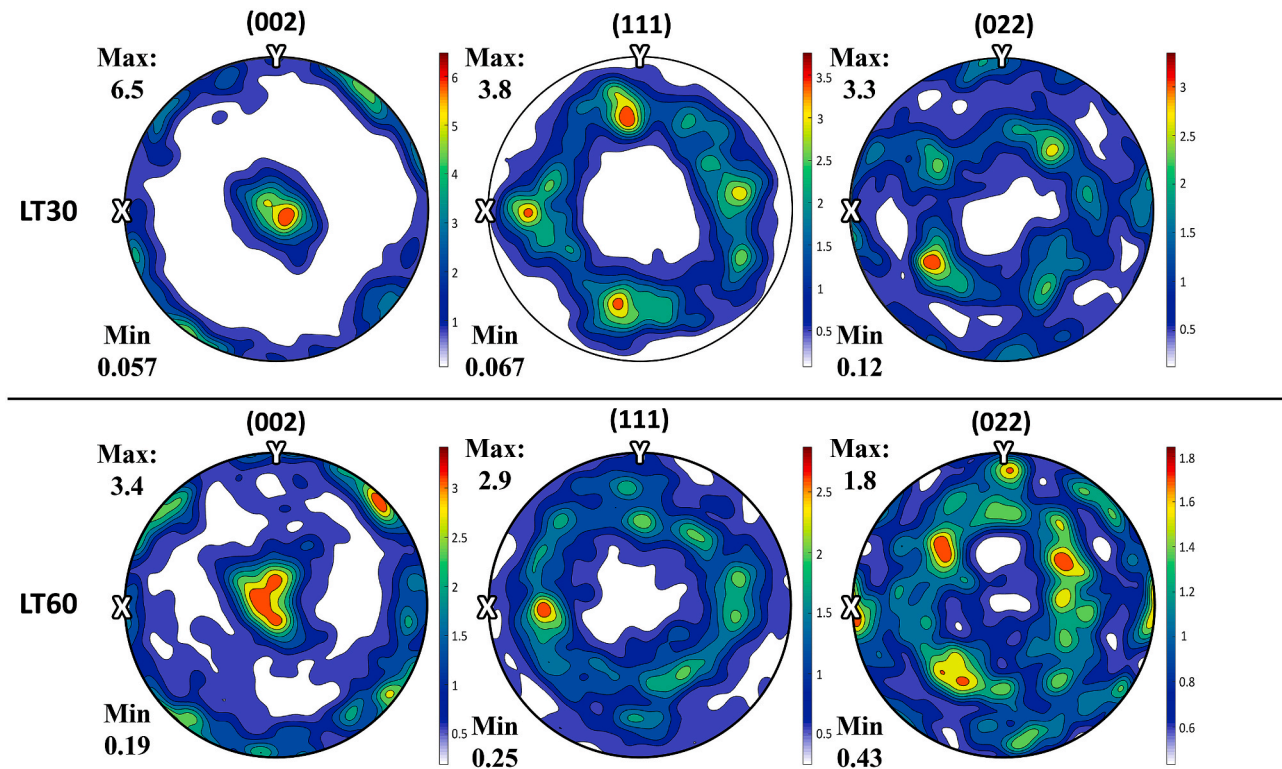

Fig. 13. Grain characterisation.

Fig. 14. Crystallographic textures pole figures (lt30 and lt60 samples).

share the same crystalline orientation <011>. Therefore, it can be concluded that side branching is the primary cause for the change from dendritic to cellular subgrain structures in these cases. The same reasoning can be applied when comparing zones B-BB, C-CC and D-DD. This behaviour is also present in the 60 μm sample, which can be observed in Fig. 12c and d in sections E-EE and H-HH. Both subgrain structures are dendritic but rotated 90°to each other, which is also caused by the side branching and zig-zag subgrain growth patterns.

It is essential to mention that the interaction of the grain growth mechanism with a low cooling rate eases the development of coarse columnar grains. For High volumetric energy density, the larger grains below the newly added layer have enough time(by the lower cooling rates) to swallow the smaller grains or select the grains with a preferred crystallographic orientation [78] similar to the seed grain orientations to follow growing(grain coarsening) in the building direction(epitaxially grain spreading across various layers) and laterally through side branching (zig-zag grain growth mechanism). In the same way, the grain coarsening promotes that crystallographic texture intensity increases because the developed crystallographic orientations get larger volumetric fractions. Then by considering the strong influence of texture intensity in material anisotropy, it is possible to infer the indirect effect of subgrain growth behaviour on the directional dependency of milling force response.

5.1.3. Grain morphology characterisation

The grain sizes and orientations of the lt30 and lt60 samples were quantified on the YZ plane. As shown in Fig. 13a, an oval profile was used to simplify the shape of the grains to measure their major and minor axes, while the grain equivalent diameter method was applied in Fig. 13d. In both cases, the grain size was more prominent in the lt30 samples than in the lt60ones.

The cumulative distribution of the grain sizes is displayed in Fig. 13a, wherein, in the lt30 sample, nearly 30% of the grains have major axis lengths exceeding 30 μm (Fig. 13 point a) and 12% exceeded 60 μm (Fig. 13 point c). In contrast, the grains in the lt60 sample are shorter

and thinner than in the lt30 sample, with 19% and 6% of grains exceeding 30 and 60 μm, respectively (Fig. 13 points b and d). Fig. 13b shows the grain aspect ratio, and it can be inferred that the lt60 grains are slenderer than the lt30 ones; this is evident when comparing Fig. 11a and g.

The grain orientation is represented by δ (see Fig. 13c). Notably, for 80% of the grains, δ lies between 0° and 20° in the lt30 sample and between 0° and 38° in the lt60 one. Therefore, it can be verified that increasing VED slows the cooling rate, thereby promoting the broadening and growth of grains through several layers. Likewise, steeper melt pool shapes favour epitaxial growth along the BD owing to higher thermal gradient values at the bottom of the melt pool.

Fig. 13d shows that the lt30 sample has a larger equivalent grain diameter distribution than the lt60 sample, which directly affects the cutting forces. The grain boundaries act as obstacles to the dislocation flow. When an LPBF-ed component is subjected to stress, dislocations originate within the active slip systems of the textured grain zone with a higher resolved shear stress. When the dislocations reach a grain boundary, they accumulate, and a local stress state is developed.

5.1.4. Crystallographic texture

The crystallographic textures of the evaluated samples are depicted in Fig. 14. The lt30 sample has a strong ring-like <001> texture with a maximum probability density of 6.5. The lt60 sample also exhibits a ring-like <001> texture, but it appears less dense (3.4 maximum probability). In the lt30 sample, it can be inferred that φ (Bunge notation) ranges from approximately 0°–15°, indicating a high density of crystalline arrangements aligned along the BD. However, the lt60 sample exhibits <111> and <011> textures on a minor scale. In both samples, the ring-like effect in the texture was caused by the laser rotation strategy.

From Fig. 14, for both samples, most of the crystals are observed to be rotated 45°to the Z-axis (ϕ_1). A second group of crystals with a lower density was rotated 70° and 5°to the Z-axis in the lt30 and lt60 samples, respectively.
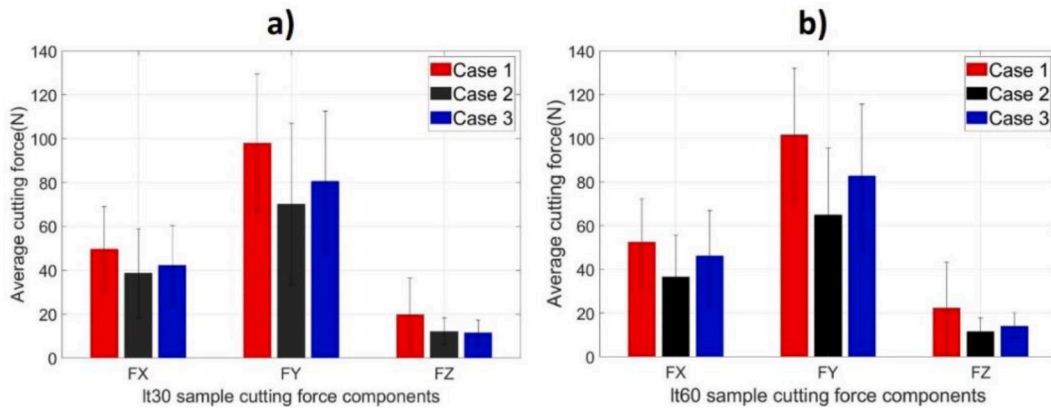
Fig. 15. Average cutting force components: a) lt30 sample; b) lt60 sample.
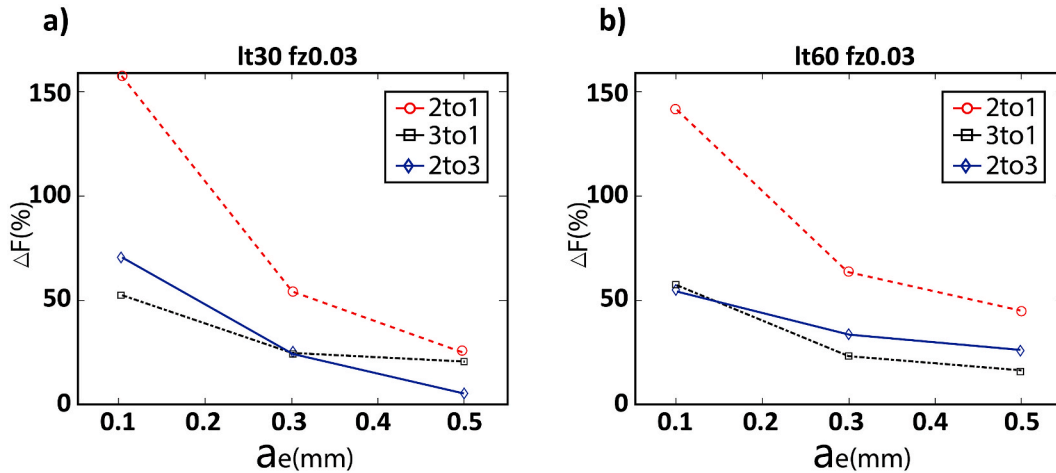

Fig. 16. Cutting force anisotropy patterns: a) lt30 sample; b) lt60 sample.

The strong correlation between the crystalline and grain orientations is an indicator of the effect of the VED on the growth of the subgrain structure. In the lt30 sample, the lower cooling rates allow a steadier growth of the grains in length and width through the zigzag growth mechanism. The influence of the melt pool on the texture is also significant; the shallower melt pools of the lt60 sample developed BD-oriented oblique grains in similar proportions to <001> and <011> textures.

5.2. Cutting force characterisation

In this section, the measured cutting force components are compared in milling cases (Fig. 9). Additionally, the specific tangential and radial cutting force coefficients for the 54 experimental conditions are presented. The analysis of homoscedasticity through Bartlett's test, the uncut chip thickness, radial depth of cut and the interaction effects of the feed rates on the variability of coefficients are also presented. Thus, the effect of the tool direction on the resultant cutting force is presented as the percent increase in the cutting force ΔF(%) when changing from one milling case to another under the same machining parameters. The same method is used to evaluate the increase in the cutting force due to the layer thickness (lt30 to lt60). Additionally, the variability in the specific cutting force coefficients ΔKt(%) and ΔKr(%) are obtained considering the percentage increase from the minimum to the maximum values of the coefficients under the same experimental conditions (layer thickness, feed rate, radial depth of cut), with the milling case being the only varying parameter. Lastly, the tangential coefficient $\overline{Kt}$ is presented as

the average of the three coefficients of the milling cases under the same experimental condition. In Section 6, the microstructural and crystallographic aspects of materials and their relationship with the cutting force variability are discussed. Appendix A (Tables 4, 5 and 6)presents the details of the components of the average and maximum forces (X, Y, Z) under each experimental condition evaluated.

Fig. 15 shows the differences between the average cutting force components by milling case. More pronounced differences and higher force levels were observed in the lt60 sample. Notably, milling cases 1 and 2 generated the highest and lowest cutting forces, respectively.

Fig. 16a and b shows ΔF(%) when the tool direction changes, according to the aforementioned cases, from cases 2 to 1, 3 to 1 and 2 to 3, respectively, for different radial depth values. The results reveal that the material anisotropy effect on the measured cutting forces is more significant when the radial cutting depth (a_e) is small, reaching values over 150% in certain cases, and it decreases as a_e increases. For a_e values of 0.5 mm, the anisotropy effect on the cutting forces decreases to a range between 5 and 25% for the lt30 sample and between 18 and 48% for the lt60 sample. The significant increase in ΔF(%) as the radial cutting depth decreases can be related to intrinsic(grain size) and extrinsic(depth of cut) size effects, which are widely reported in literature as root causes of specific cutting force variability [79,80]. However, the difference between the 2to1, 3to1, and 2to3 curves means that the increased ΔF(%) values were not homogeneous. the largest difference was observed while changing from cases 2 to 1 in all scenarios and the change from cases 3 to 1 exhibited the smallest difference. It suggest that material anisotropy plays an important role in maximizing or minimizing these size effects.
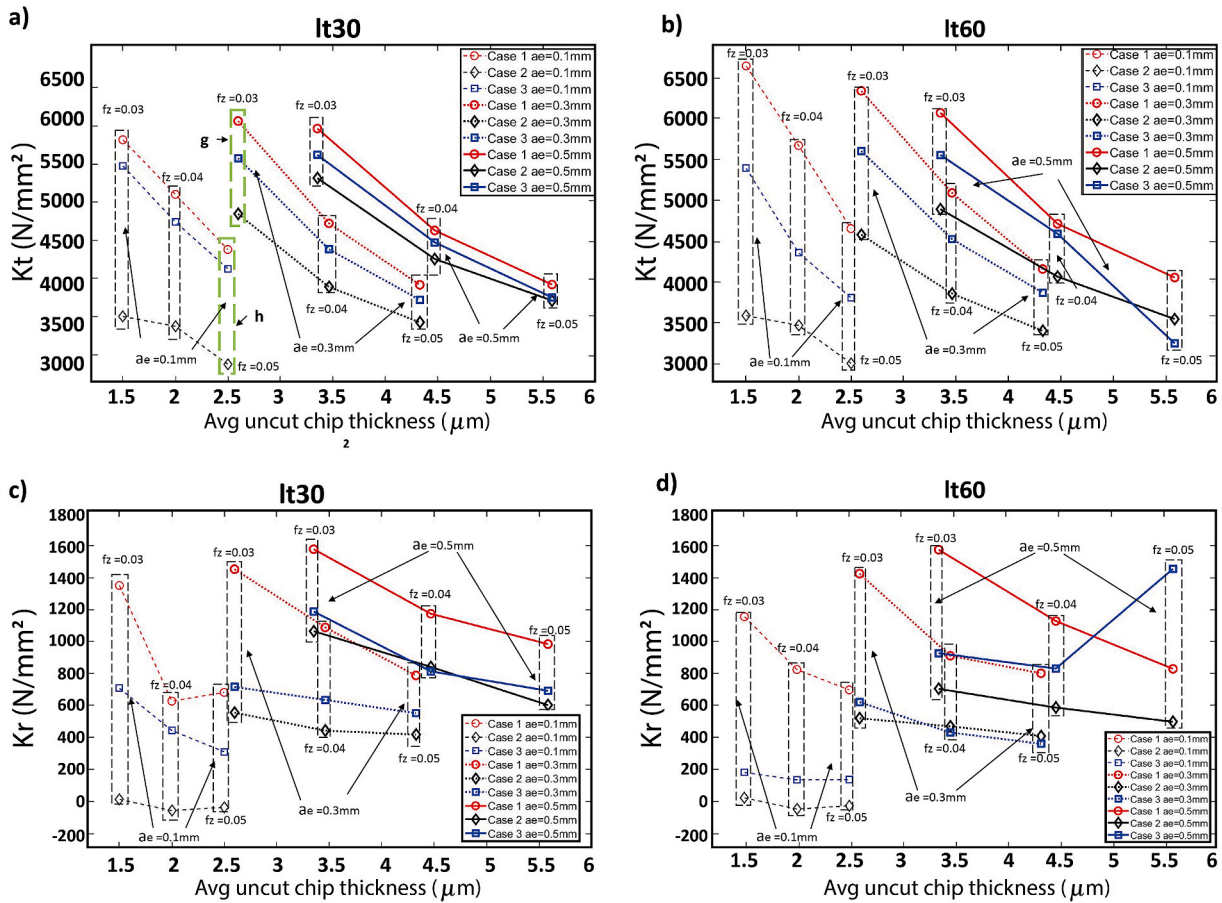
Fig. 17. Tangential and radial cutting force coefficients as functions of the average uncut chip thickness: a) Kt for the lt30 sample; b) Kt for the lt60 sample; c) Kr for the lt30 sample; d) Kr for the lt60 sample.
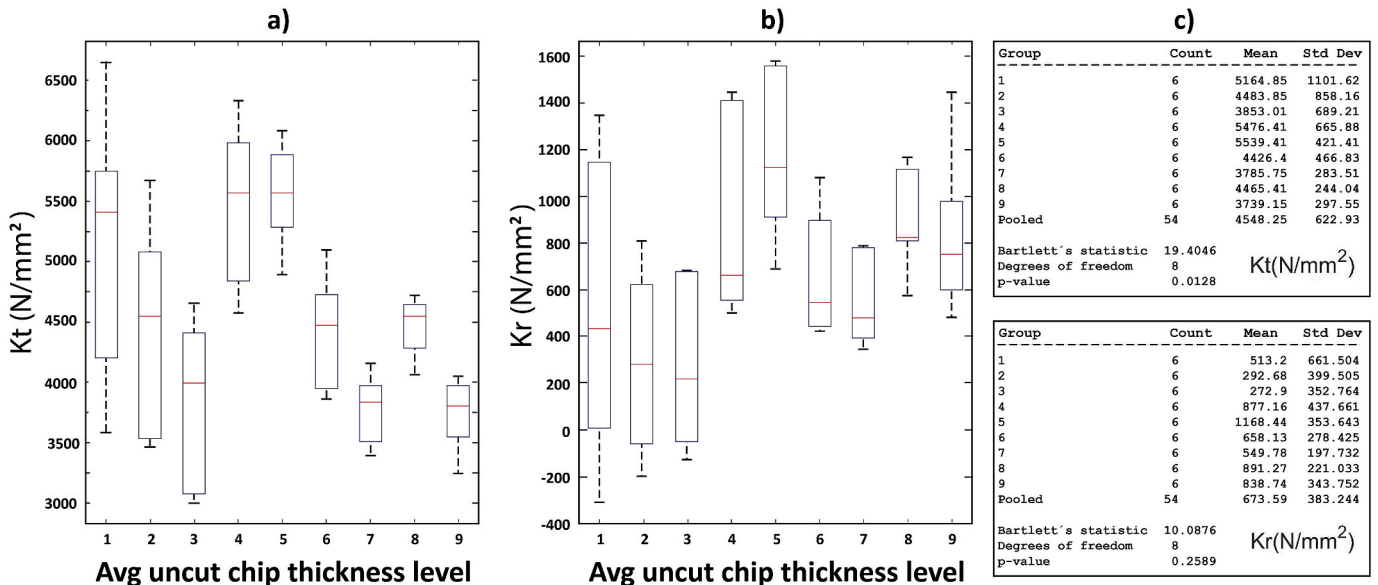
Fig. 18. Kt and Kr Bartlett's test analysis: a) Box-whisker plot for Kt; b) Box-whisker plot for Kr; c) Statistical details regarding Bartlett's test.

The energy criterion was used to compare the effects of anisotropy on the cutting forces in both samples, suggesting that the lt60 sample requires 37% more cutting energy than the lt30 sample (this topic is discussed extensively in Section 6.2).

Fig. 17 shows the tangential (Kt) and radial (Kr) cutting force coefficients for the lt30 and lt60 samples as functions of the average uncut chip thickness under the 54 experimental conditions evaluated. Each figure comprises three groups of nine coefficients corresponding to
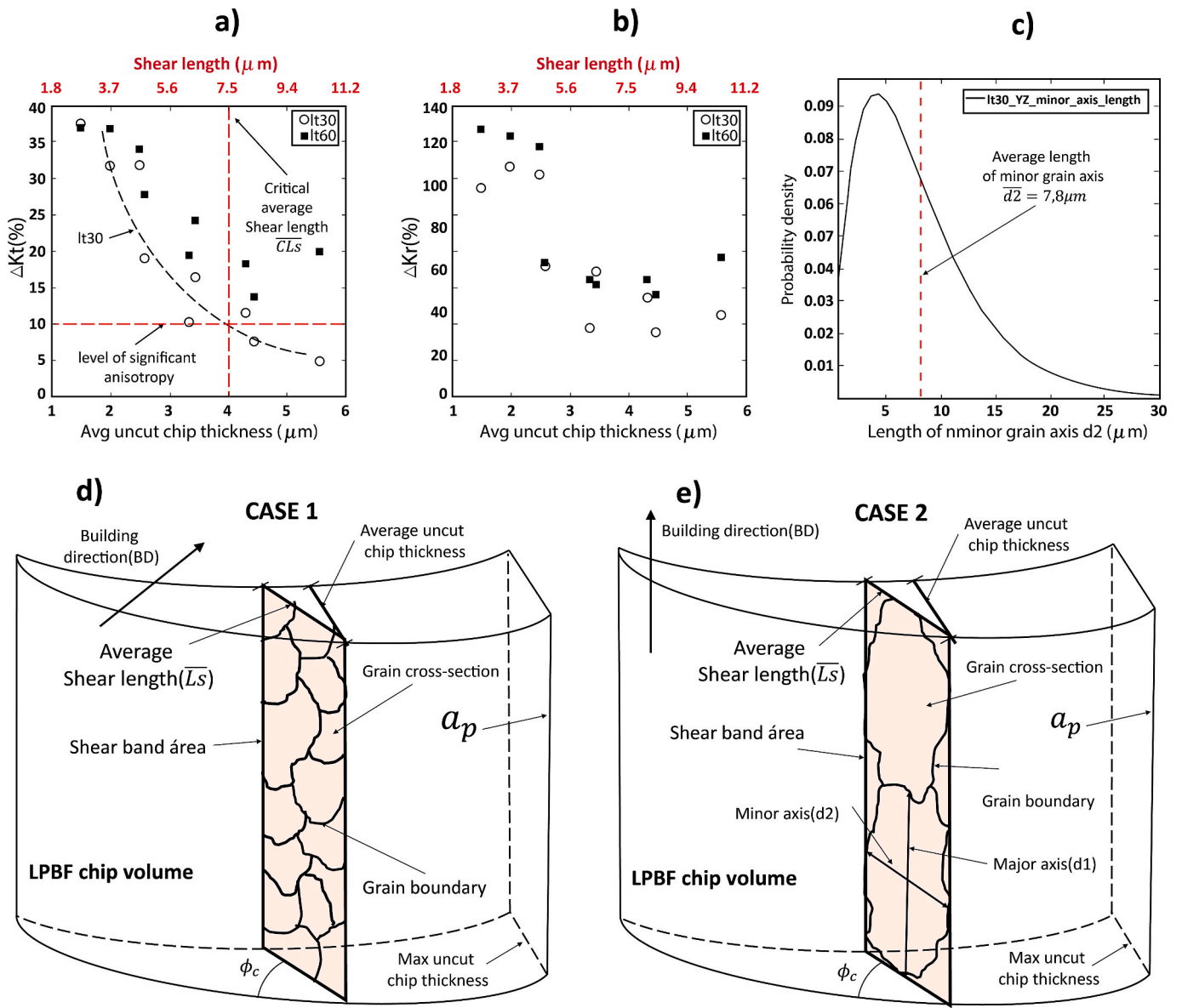
Fig. 19. Correlation between $\overline{CLs}$ and d2: a) ΔKt (%); b) ΔKr (%); c) Length of minor axis of the grain for the lt30 sample in the YZ plane; d), e) Details of the grain cross-section scheme in the shear band area for cases 1 and 2.

Fig. 20. f_z and a_e interaction effects on Kt: a) Effect on ΔKt (%); b) Effect on $\overline{Kt}$.

different a_e values (0.1, 0.3 and 0.5 mm). Within each group, the co-efficients are further grouped according to the corresponding feed rates (0.03, 0.04 and 0.05 mm/rev). Lastly, each feed rate group is formed by the coefficients corresponding to each milling case.

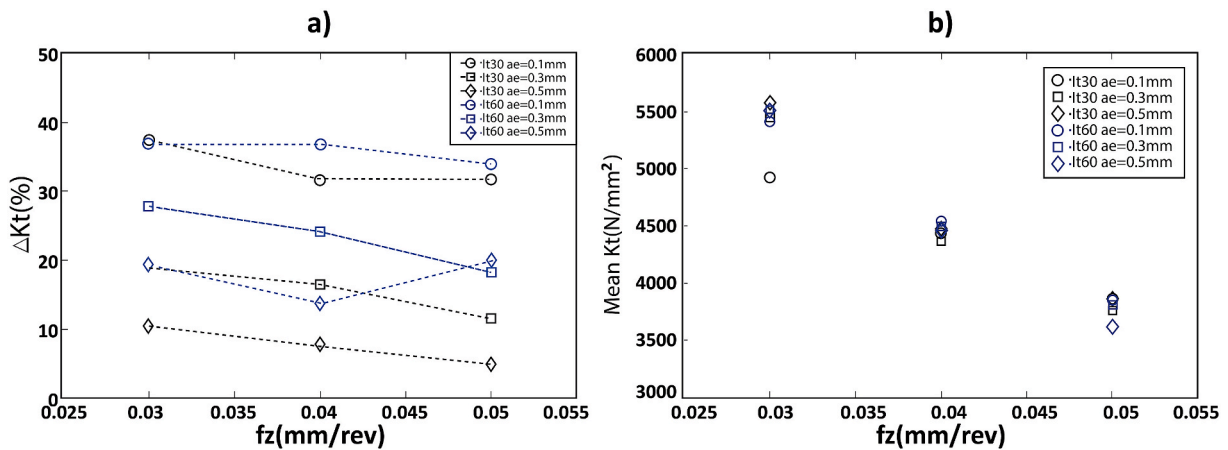Notably, at lower average uncut chip thicknesses, the variability of the tangential coefficients increased significantly. However, this effect was more pronounced in the lt60 sample than in the lt30 one (Fig. 17a and b). The effect of the average uncut chip thickness on the dispersion of Kr is much smaller; however, the variability of Kr within the feed rate group coefficients is larger than that of the Kt coefficients for all uncut chip thickness levels. Some cutting force coefficients for traditionally produced Inconel 718(cast and forged) are compared with LPBF cutting force coefficients from this research in appendix A, table 7.

From Fig. 17a, it is evident that the difference between the co-efficients of cases 1 and 3 remains nearly constant for all the evaluated levels. However, milling case 2 was more sensitive to reductions in the uncut chip thickness, which can be observed by a decrease in the co-efficients. On the other hand, for the lt60 sample, the decrease in chip thickness can be observed to affect the dispersion of the tangential co-efficients Kt for the three milling cases in a similar ratio.

Fig. 18 corresponds to the Bartlett's test conducted to evaluate the variances of the Kt and Kr coefficients with respect to the average uncut chip thickness. Box-whisker plots for Kt and Kr are shown in Fig. 18a and b, respectively. Fig. 18c shows the details of the statistical analysis using Bartlett's test, where P-values of 0.0128 and 0.25 for Kt and Kr, respectively, were observed. This indicates that the Kt coefficients do not correspond to a normal distribution having significant differences between the variances of each level. While the Kr coefficients adhere to the assumption of normality related to homoscedasticity, consequently, the level of anisotropy observed in the tangential coefficients is very sensitive to the uncut chip thickness. In contrast, the levels of anisotropy in the radial coefficients were similar at all uncut chip thickness levels.

Fig. 19a and b shows the distribution of ΔKt (%) and ΔKr (%) with respect to the uncut chip thickness. From Fig. 19a, it is possible to infer a relationship between the decrease in ΔKt (%) and the increasing average uncut chip thickness for both samples. Considering a 10% variation in the coefficients as a control value for evaluating the significance of material anisotropy in the milling process and also that ΔKt (%) is an indicator of material anisotropy, it can be concluded that, for the lt30 sample, the anisotropy is significant for values equal to or less than a 4 μm average uncut chip thickness. However, for the lt60 sample, the anisotropy levels were significant at all uncut chip thickness levels evaluated. This value is hereafter referred to as the *critical average uncut chip thickness* to facilitate further analysis.

It is essential to consider the direct relationship between the average uncut chip thickness, shear angle and average shear length $\overline{Ls}$. For the lt30 sample, it can be established that the critical average uncut chip thickness (4 μm) corresponds to $\overline{Ls} = 7.5$ μm (See vertical red dashed line in Fig. 19a), considering $\varphi_c = 33$ °according to the analysis of the effective Taylor factor. Similarly, the value of $\overline{Ls} = 7.5$ μm is hereinafter referred to as the critical average shear length $(\overline{CLs})$ for case 2 in the lt30 sample.

The alignment of columnar grain growth with the BD allows the correlation of the grain dimensions (major and minor axes) with certain milling parameters. For milling case 2, a relationship between the major axis length of the grain $d1$ and a_p can be established because both magnitudes are oriented on the Z-axis (BD). In a complementary manner, the minor axis length of the grain $d2$ could be related to $\overline{Ls}$ (see Fig. 19e). Analysing the grain dimensions of the lt30 sample demonstrates a correlation between the average length of the minor axis of the grain (7.8 μm, see Fig. 19c) and $\overline{CLs}$ (7.5 μm, see Fig. 19a, c, 19d and 19e). This suggests that the difference between the tangential co-efficients of milling cases 1 and 2 may be significant when $\overline{Ls} \leqslant d2$.

Fig. 19b shows significant levels of anisotropy in the radial co-efficients for all uncut chip thickness levels. However, notably, there are

two groups of ΔKr (%) values: the first group with values higher than 100% and chip thicknesses between 1.5 and 2.5 μm corresponding to the tests with lower radial depths of cut ($a_e = 0.1$ mm) and the second group with ΔKr(%) values ranging from 30 to 65% under the remaining experimental conditions evaluated. In both cases, the ΔKr(%) values were similar, which agrees with Bartlett's test.

The feed rate plays an important role in determining the value of the cutting force coefficients (radial and tangential) beyond its direct relationship with the uncut chip thickness. From Fig. 17, it is observed that there are groups of different feed rates with very similar uncut chip thicknesses (i.e. points h and g, Fig. 17a outlined by dashed green lines), but with significant differences in their coefficients. In all instances, the groups with higher feed rates can be observed to have lower coefficient values. In this regard, Fig. 20a shows the effect of the interaction between f_z and a_e on ΔKt (%). It is observed that for all levels of a_e and both samples (lt30 and lt60), f_z has no significant effect on ΔKt (%). However, from Fig. 20b, it can be seen that f_z plays a significant role in determining the mean value of the tangential coefficients $(\overline{Kt})$ while a_e is irrelevant. Thus, it can be concluded that the relationship between the uncut chip thickness and the ΔKt (%) variability is mainly due to a_e, while the variation in $(\overline{Kt})$ is mainly due to the feed rate.

6. Discussion

From Section 5.2, three main issues can be established. The first is related to the variability (anisotropy) in the radial and tangential co-efficients due to the change in tool position (milling cases) for each combination of f_z and a_e. The anisotropy is observed under all the experimental configurations analysed, and it is significant for Kt over the entire range of the average uncut chip thicknesses considered for the lt60 sample and for values equal to or lower than 4 μm for the lt30 sample under the established control parameter. In the case of Kr, the anisotropy was significant under all the experimental conditions evaluated. The second issue is related to the relationship between the level of anisotropy [ΔKt (%) and ΔKr(%)] and the average uncut chip thickness, where an inversely proportional relationship between anisotropy and the uncut chip thickness was observed for the tangential coefficients. The third issue pertains to the effect of f_z on $\overline{Kt}$, where it can be observed that increasing the feed rate decreases Kt for any value of a_e in both samples. This aspect, however, is not related to the anisotropy of the material, as shown in Fig. 20a. This behaviour (third issue) can be explained using the effect of the increase in f_z on the increase in the cutting temperature, which, in turn, decreases the plastic flow stress $\acute{\sigma}_y$ (temperature softening). Consequently, a decrease in $\acute{\sigma}_y$ leads to a decrease in the values of the cutting forces. Although it is present in the experimental results, the third issue will not be discussed further in this section because it is not relevant to the analysis of the effect of material anisotropy on the cutting forces.

The observed correlation between the significantly high anisotropy control level, the average critical shear length and the average minor axis length of the grain indicates that the directional dependency of the cutting forces in the shear band may partially depend on how large the fraction of the cutting force resulting from the crystal shear strength $R_{Crystal}$ (slip within the grain) is compared to that resulting from the grain boundary strength $R_{Boundary}$ (slip across grain boundaries). This process of restricting dislocation movement across grain boundaries forms the basis of the grain boundary strength effect [81].

Namely, the development of significant levels of anisotropy (i.e. the cutting force variation between cases 2 and 1 when $\overline{Ls} \leqslant d2$) is related to the interactions of both tool positions with the microstructure. In this regard, the corresponding tool position in case 2 favours a fraction of the cutting force due to the crystal shear strength that is considerably higher than that due to the grain boundary strength ($R_{Crystal} \gg R_{Boundary}$); i.e., the slip deformation mode mainly develops inside the grains and at a much lower level across the grain boundaries. However for the tool position in
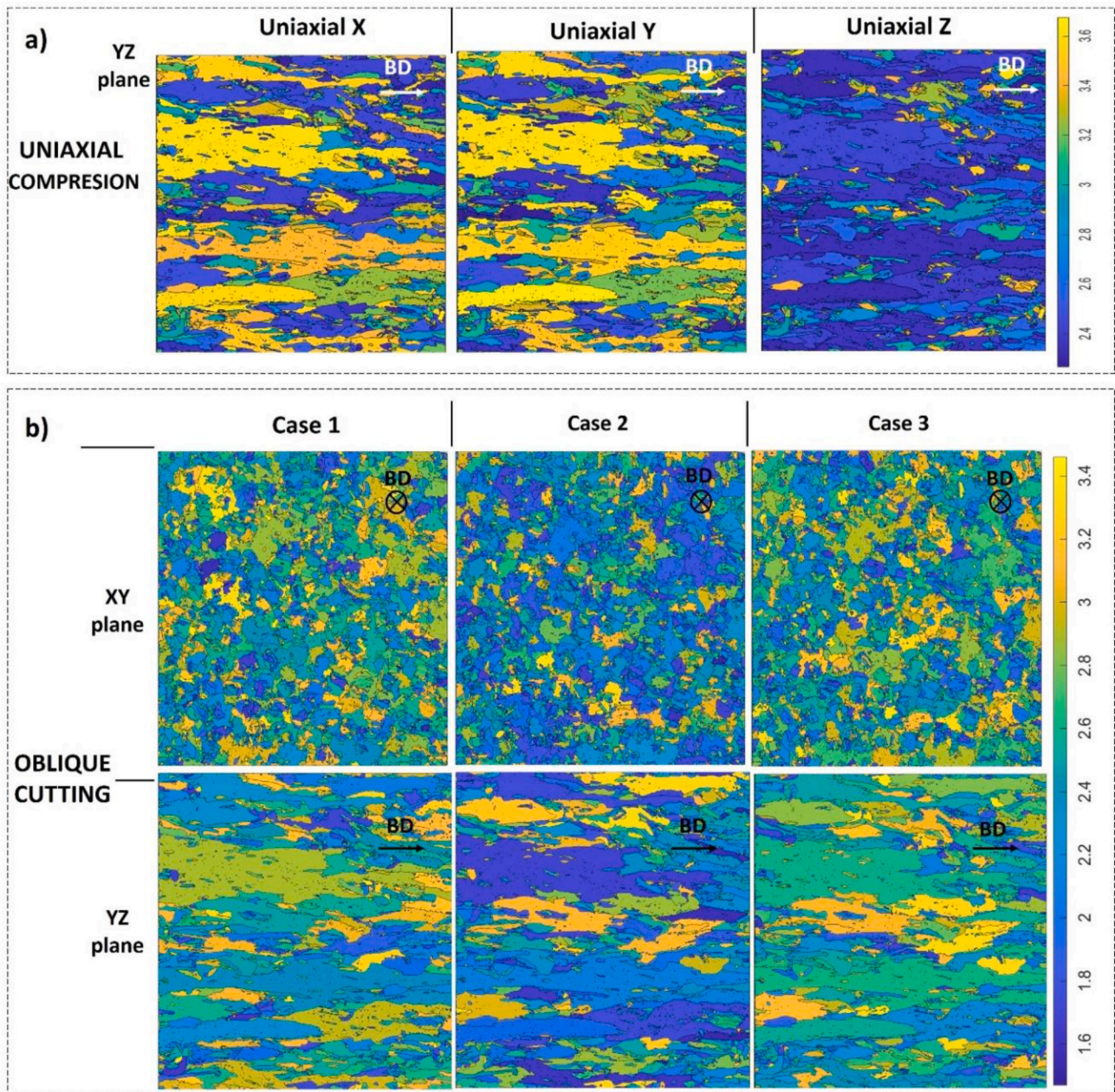
Fig. 21. a) Uniaxial compression Taylor factor by grains–lt30 sample; b) Oblique cutting Taylor factor by grains–lt30 sample.

case 1, $R_{Crystal} \approx R_{Boundary}$ (because the XY plane has a more extensive fraction of the equiaxed grain structure owing to the columnar grain cross-section compared to the YZ plane). This implies that for $\overline{Ls} \lessdot d2$, milling case 2 resembles the milling of single-crystalline materials, where the grain boundary density is much lower than those of poly-crystalline materials [82]. However, milling case 1 resembles the milling of a polycrystalline material.

Based on the discussion above, the directional dependency of the measured milling forces and their variabilities are analysed in terms of the crystallographic and grain morphology effects with the Taylor factor and grain boundary density, respectively.

6.1. Anisotropy in shear strength by crystallographic effect

The high level of the <001> ring-like texture intensity observed in Fig. 14 indicates the necessity to consider the crystallographic effect as a cause of anisotropy concerning the cutting forces related to the

machining cases. Therefore, the distribution of the Taylor factor was calculated using the measured ODF, obtained using EBSD, and the DODF from the orientations with the highest volumetric fraction. The tool geometry, tool positions and the pole figure pattern were considered, and the model proposed in Equations (2)–(19) was employed.

Fig. 21 shows the Taylor factor for uniaxial compression and oblique cutting. For this purpose, the statistical distribution of the Taylor factor in each crystal orientation of the grains was calculated using the model proposed in Equations (2)–(19) for oblique cutting (Fig. 21b). Fig. 21a shows the Taylor maps under three uniaxial compressive loads for the lt30 sample, and although the X- and Y-axes show similar distributions, the one along the Z-axis is significantly different. The lower Taylor values of the Z-axis imply lower shear strengths of the material by uniaxial Z load related to the X or Y directions. The observed ring-like textures resulting from the rotation scanning strategy can explain the similarity between the uniaxial Taylor factors in the X and Y directions. Meanwhile, the low shear strength across the Z-axis indicates that the
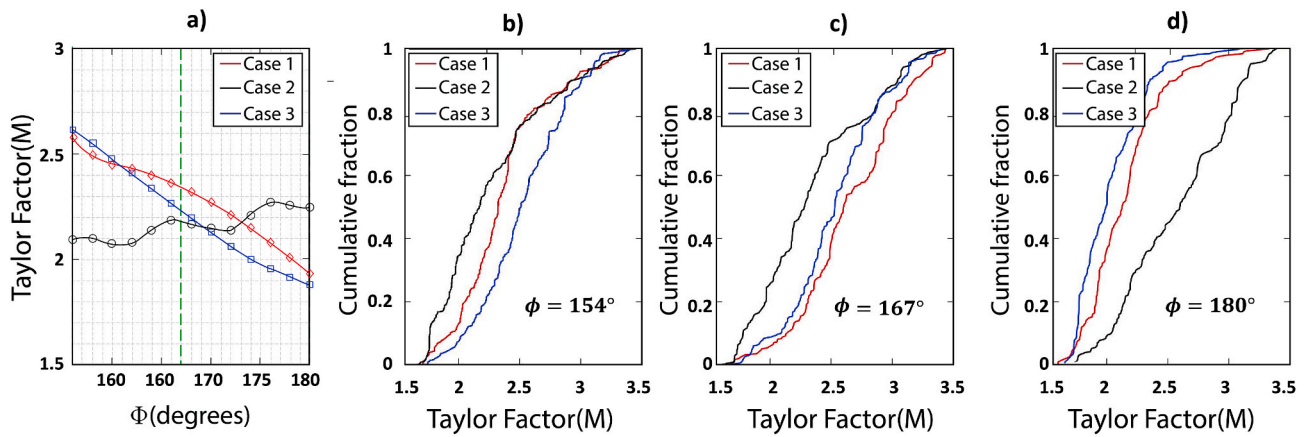
Fig. 22. a) Macroscopic Taylor factor obtained from the DODF in the function of the engagement angle ϕ; b), c), d) Single-crystal Taylor factor distributions by ODF when ϕ=154°, 167° and 180°, respectively.
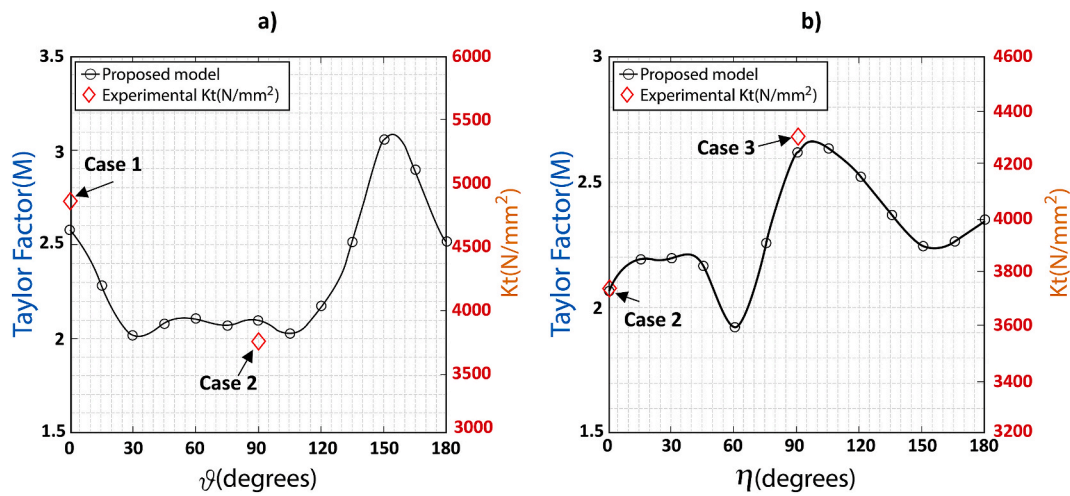
Fig. 23. a), b) Fluctuations in the macroscopic Taylor factor prescribed by rotations of the tool by ϑ and η, respectively, obtained from the proposed model and compared with the experimental Kt for each milling case.
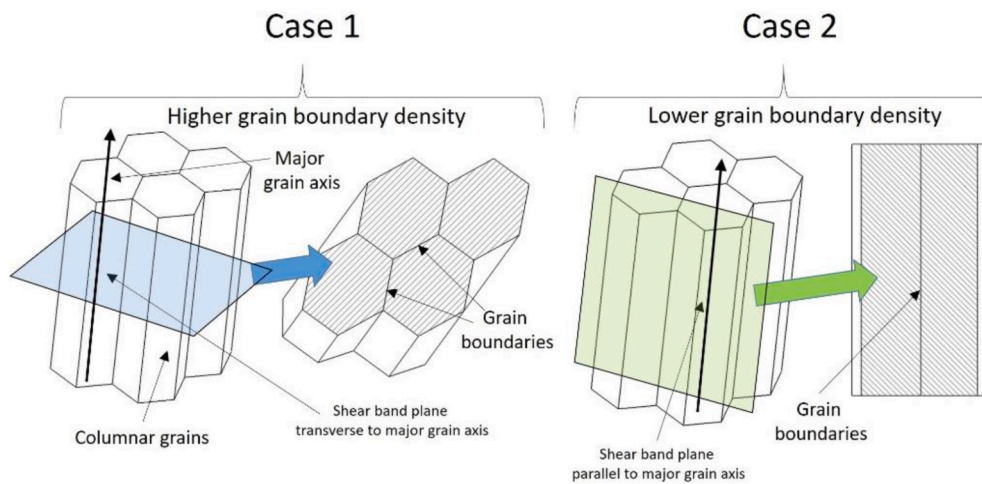
Fig. 24. Effect of the shear band orientation on the grain boundary density scheme.
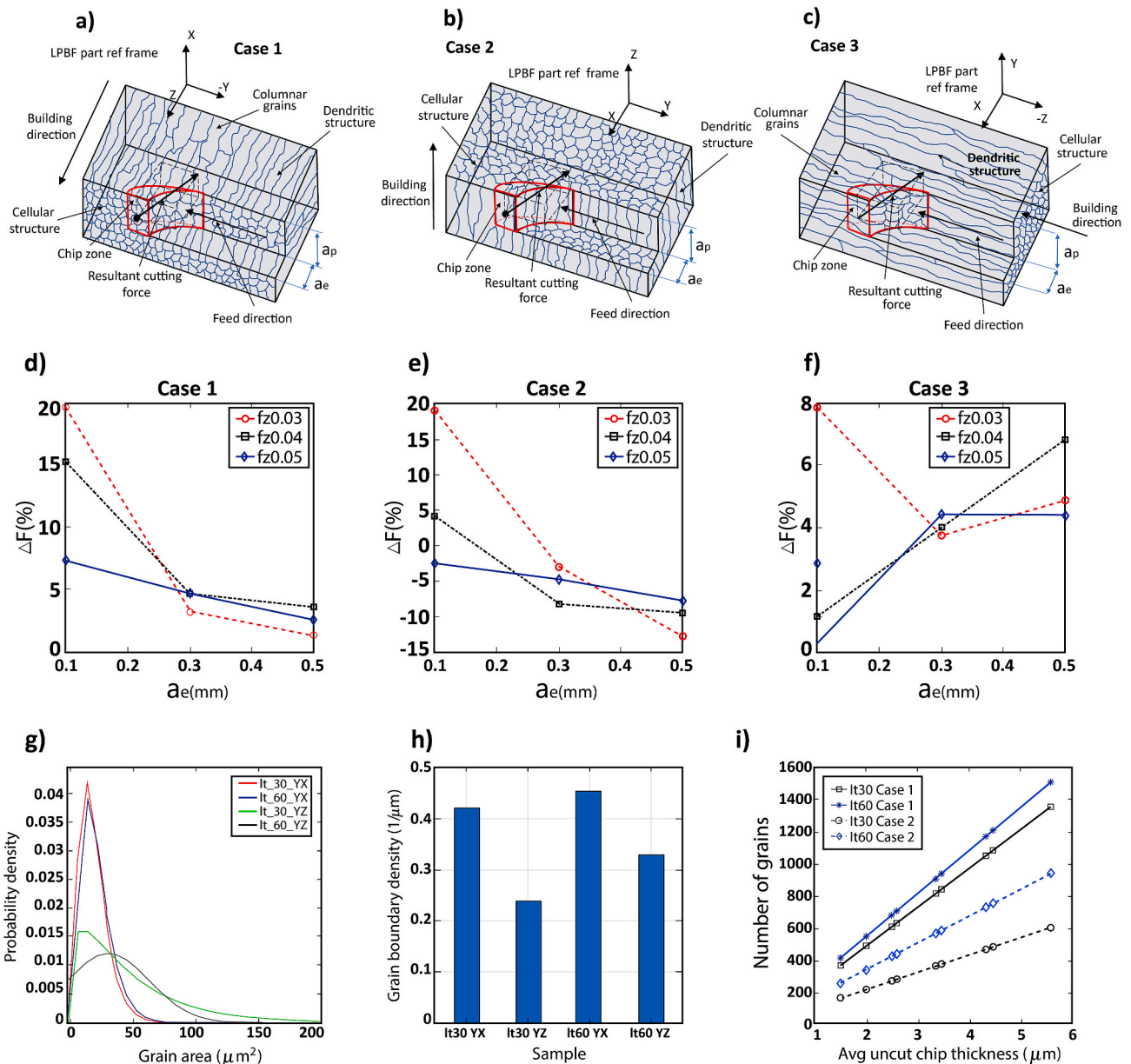
Fig. 25. a), b), c) Representation of the milling cases; d), e), f) percent increment in cutting force by grain refining; g) Grain area distribution by sample; h) Grain boundary density (GBD) by sample i) Number of grains in the function of average uncut chip thickness.

epitaxial growth along the BD is not completely prevented with a laser rotation strategy. The similarity between the uniaxial X and Y Taylor values implies that this material can be classified as transversely isotropic in many cases.

Fig. 21b shows a comparison between the Taylor factors in each grain under oblique loads for each milling case in the lt30 sample when $a_e = 0.5$, $\beta = 30°$ and $\phi_c = 35°$ (instant of the first contact between the tool and workpiece). The blueish colour of the case 2 maps (XY and YZ) indicates that the lower shear strength for peripheral milling occurs when milling case 2 is applied; this is corroborated by the experimental cutting forces. A comparison between the Taylor's cumulative

distribution for different milling cases for the lt30 and lt60 samples is displayed in the appendix (Fig. 26).

Fig. 22a shows the macroscopic Taylor factor for each milling case and engagement angles ranging from 154° to 180° (see Fig. 7) for the lt30 sample. Fig. 22b, c, and 22d represent the statistical distribution of the Taylor factor corresponding to the crystalline orientation of each grain present in the sample. The value of the macroscopic Taylor factor is observed to be similar to the mean value of the distributions in Fig. 22b, c, and 22d. This is an important aspect when considering that the machining process is a macroscopic one, and a representative magnitude of the crystalline distribution is required for comparing the

resistance to cutting owing to the tool position. Fig. 18a shows a significant difference in the level of case 2 with respect to cases 1 and 3. However, as the engagement of the tool with the material progresses, the level of resistance to cutting can be observed to decrease for cases 1 and 3 and increase for case 2. The differences between the Taylor factor in cases 2 and 1 are noticeable; however, the levels for cases 1 and 3 are similar. The overall mean Taylor factor obtained was the highest for case 1, followed by case 3, and case 2 exhibited the lowest one. This agrees well with the measured cutting force levels.

Fig. 23 shows the variation in the macroscopic Taylor factor (polycrystalline) for different tool positions according to its rotation on the Y- (ϑ angle; Fig. 23a) and X-axes (η *angle*; Fig. 23b) (for details regarding ϑ and η, see Fig. 9) compared to the tangential cutting force coefficient (Kt). The trend in the Taylor factor is observed to be similar to the one in the Kt (the same was observed for the average cutting forces). Fluctuations in the Taylor factor are associated with changes in the alignment of the strain tensor to the crystalline slip systems, considering that the vast majority of grains have a crystalline orientation aligned with the manufacturing direction (BD).

6.2. Effect of grain size and grain morphology on cutting forces

It is well known that the cutting forces depend on the mechanical properties of the material, and the yield stress is a relevant parameter. During plastic deformation, dislocations move through the crystalline arrangement within alloy grains until they reach a grain boundary. At this point, the large atomic mismatch between the different grains creates resistance to dislocation. Reduction in the grain size leads to a higher grain boundary density (ρ), creating further resistance to the dislocation movement and, in turn, strengthening the material. The Hall–Petch law outlines the effect of the grain size on the yield strength (see Equation (21)).

$$\sigma_y = \sigma_0 + \frac{k_y}{\sqrt{d}}, \qquad (21)$$

where σ_y is the yield stress, d is the equivalent grain diameter, and σ_0 and k_y are material constants. Thus, k_y represents the Hall–Petch slope of the yield stress function with respect to the grain orientation (δ). The Hall–Petch slope is generally higher in <100> textured materials than in <110> ones. This could be the consequence of a low density of dislocation sources combined with a lower density of high disorientation angle of grain boundaries (HAGBs) and the difficulty of activating the grain boundary shearing process [83].

The grain dimensions shown in Section 5.1 indicate a predominant columnar morphology. Therefore, this shape implies that grain diameter is not the most appropriate concept to consider. Considering that the grain boundary density is defined as the total perimeter of the grain boundaries divided by the evaluated area [84] and that the cutting action is developed from the theory of the plane of a shear band, the grain orientation relative to this plane produces variations in the effective grain boundary density when changing the tool position (see Fig. 24).

Fig. 25a, b and 25c represent the grain orientation relative to the chip zone for each milling case. Evidently, case 1 implies that grains are mainly cut transversely, while case 2 represents a shear plane that is more aligned with the grain orientation. Case 3 represents an axial cut at the beginning and a transverse cut at the end of the engagement. These aspects are crucial to understanding the effects of grain morphology on the cutting forces.

Fig. 25d, e, and 25f show the percentage increase in the cutting forces ΔF(%) when milling the lt60 sample compared to when milling the lt30 sample under the same machining parameters; each graph corresponds to a milling case representing an increase in the cutting force in most cases. This increase is small because the radial depth of cut and feed increase for case 1, but the pattern is different for cases 2 and 3.

Fig. 25g shows the grain area distribution, considering an ellipsoid shape for the YZ and XY sample planes (based on the d1 and d2 distributions). The average grain areas for the lt30 sample are 46.81 μm^2 and 20.73 μm^2 for the YZ and YX planes, respectively, while those for the lt60 sample are 29.8 μm^2 and 18.6 μm^2 for the YZ and YX planes, respectively. Fig. 25h shows the grain boundary densities for the YZ and XY planes in lt30 (0.42 μm^{-1} in the XY plane and 0.23 μm^{-1} in the YZ one) and lt60 (0.45 μm^{-1} in the XY plane and 0.34 μm^{-1} in the YZ one). Considering the decreased average grain area and the increased grain boundary in both planes in the lt60 sample compared to those in the lt30 one, the increased development of grain refining in the lt60 sample compared to that in the lt30 sample can be confirmed. The observed increment in the grain boundary density of lt60 sample correlates with the increase in the cutting force for milling cases 1 and 3 under all experimental conditions; this increment is more pronounced in milling case 1. Fig. 25i depicts the number of grains in the plane of the shear band as a function of the average uncut chip thickness considering the average grain area values from Fig. 25g. the number of grains per uncut chip thickness in both samples evidently increases to a greater extent for case 1 than for case 2.

In case 2, grain refining produced an effect contrary to that expected because the cutting forces decreased under most experimental conditions. This phenomenon had been reported by Papanikolaou et al. [85], who concluded that grain boundary sliding is the root cause. To understand this unique behaviour, it is important to consider two conditions: the first is that for case 2, the major axis of the grain is nearly parallel to the milling tool axis (Fig. 25b), and the cutting edge encounters parallel grains with smaller grain sizes. Furthermore, such an encounter could promote an increase in the grain boundary sliding strain mode to the detriment of the slip strain mode compared to cases 1 and 3. Considering that grain boundary sliding mainly develops when the grain size is less than 10 μm [86], which is the case for the lt60 sample. the lack of intragranular shear of larger grains (by slip strain mode), as in cases 1 or 3, could constitute one of the reasons for the lower milling forces in case 2 when milling the lt60 sample.

Based on the above discussion, it is possible to define the cause of the increased anisotropy in cutting forces when machining the lt60 sample compared to when machining the lt30 one based on the differentiated effect that grain refinement has on cases 1 and 2. This is because grain refinement increases the level of cutting force in case 1 owing to an increased grain boundary density (where the slip strain mode occurs by intragranular shear). However, in case 2, grain refinement decreased the cutting force because the tool position with respect to the grain orientation favours the development of the grain boundary sliding mode.

7. Conclusions

This study analyses the effect of LPBF process parameters on the anisotropy of AM-ed parts as well as on cutting forces during the milling of such parts. The main relationships between LPBF, microstructure and machining were explained through the analysis and characterisation of the alloy microstructure and texture. A model that considers the

crystalline orientation distribution function, texture pole figure patterns (associated with LSSs), tool position, and tool geometry was proposed to calculate the Taylor factor in LPBF components under oblique cutting conditions. The model demonstrated a good correlation between the Taylor factor distribution and the measured cutting forces.

The main results are summarized as follows:

- The directional dependency of the milling force is closely related to the interaction between the orientation of the plane of the shear band (due to the relative tool position with respect to the workpiece), predominant crystalline textures, and orientation and size of the LPBF-printed columnar grains.
- The effect of material anisotropy on the variation of cutting forces as a function of tool position can be explained and quantified through the crystallographic and grain morphology effects. High-VED manufactured parts are associated with steeper melt pools, columnar grains closely aligned with the BD and dense crystallographic textures. For which, quantification of the crystalline effect on the shear strength through the Taylor factor enables a good prediction of the trend in the cutting force fluctuation at various tool positions. However, low-VED manufactured parts are associated with multiple crystalline orientations, implying that the crystallographic effect on the cutting force is smaller, rendering the grain morphology effect more relevant. The proposed model could be expanded to accommodate different cutting tool geometries and/or BCC lattice materials with the necessary modifications.
- A relationship was observed between the uncut chip thickness and the variability in the tangential cutting force coefficients with respect to the tool position. In the case of the high-VED sample, significant levels of anisotropy were observed to occur under experimental conditions with an average shear length equal to or less than the length of the minor axis of the columnar grains.
- The effect of grain morphology (grain size, grain shape and orientation) on the cutting force was evaluated using grain boundary density analysis, which allows the evaluation of the effects of material anisotropy on the cutting forces when the crystallographic effect is weak. Indeed, a correlation was obtained with the measured cutting force levels for both the low-and high-VED printed parts.

- The low-VED manufacturing conditions increase the grain boundary density. Considering the possible development of the grain boundary sliding mode for small grains ($<10 \ \mu m$), cutting forces were lower when the tool axis was parallel to the columnar grain major axis (or BD). Conversely, the highest cutting forces occurred when the tool position generated planes of the shear bands transverse to the major axis of the columnar grains.

Credit

José David Pérez: Conceptualization; Data curation; Formal analysis; Investigation; Methodology; Project administration; Visualization; Roles/Writing - original draft. Pr. Luis Norberto López de Lacalle: Conceptualization; Formal analysis; Methodology; Funding acquisition; Project administration; Resources; Software; Supervision; Dr. Gorka Urbikain: Conceptualization; Formal analysis; Methodology; Project administration; Supervision; Roles/Writing - original draft. Octavio Pereira: Investigation; Formal analysis; Methodology; Supervision; Roles/Writing - original draft. Silvia Martínez: Investigation; Methodology; Supervision. Jorge Bris: Funding acquisition; Project administration; Supervision.

Declaration of competing interest

The authors declare that they have no known competing financial interests or personal relationships that could have appeared to influence the work reported in this paper.

Acknowledgments

A. Appendix: cutting forces by experimental conditions, predicted shear angles, and single crystal Taylor distributions

Table 4
Data on the measured cutting forces and experimental conditions of milling case 1

ae (mm)	t (μm)	fz(mm/rev)	FX_mean (N)	FY_mean (N)	FZmedia (N)	FX_MAX (N)	FY_MAX (N)	FZ_MAX (N)	avg uncut chip thickness (μm)	Kt(N/mm^2)	Kr(N/mm^2)
0,1	30	0,03	21,71	50,5	4,8	92,75	149,8	24	0,0015	5745,75	1351,45565
0,1	30	0,04	27,31	57,55	9499	125,3	160,6	43	0,002	5079,50707	627,165441
0,1	30	0,05	32,55	61,74	9741	131	179	47,8	0,0025	4406,14814	682,242292
0,3	30	0,03	45,73	97,95	13,66	163,6	268,8	61,6	0,002598	5974,51888	1453,5601
0,3	30	0,04	52,96	99,97	14,19	175,5	280,6	62	0,0034641	4726,48832	1089,13379
0,3	30	0,05	52,04	119,3	19,4	192,2	287,3	68	0,0043301	3975,18289	788,404365
0,5	30	0,03	63,56	125,8	17,61	199	345	66	0,0033541	5883,23021	1578,95517
0,5	30	0,04	70,88	132,9	21,1	213,6	358,4	72,3	0,0044721	4639,53264	1174,48309
0,5	30	0,05	79,6	137	24,05	230,7	382,4	81,1	0,0055901	3978,31813	984,359583
0,1	60	0,03	24,88	61,56	7,84	116	164,4	39	0,0015	6642,38676	1146,54607
0,1	60	0,04	30,41	67,16	8636	136,6	182,5	50,2	0,002	5669,36238	815,49274
0,1	60	0,05	31,13	68,21	9895	139,5	187,9	57	0,0025	4653,46097	687,927645
0,3	60	0,03	49,41	99,93	14,29	178,1	280,6	62,6	0,0025980	6337,90891	1416,2539
0,3	60	0,04	55,83	104,2	7,6	202,1	289,1	46	0,0034641	5090,22377	901,566506

Table 4 (*continued*)

ae (mm)	t (µm)	fz(mm/rev)	FX_mean (N)	FY_mean (N)	FZmedia (N)	FX_MAX (N)	FY_MAX (N)	FZ_MAX (N)	avg uncut chip thickness (µm)	Kt(N/mm^2)	Kr(N/mm^2)
0,3	60	0,05	62,16	107,6	17,23	203,1	298,6	70,4	0,0043301	4159,22681	791,720472
0,5	60	0,03	64,08	127,3	19,46	208,2	353	74,2	0,0033541	6069,2441	1565,97745
0,5	60	0,04	74,28	137	22,61	221,5	359,5	84,9	0,0044721	4712,53228	1119,32781
0,5	60	0,05	80,08	141,2	25,14	249,3	375,6	90,3	0,0055901	4054,88664	819,54262

Table 5
Data on the measured cutting forces and experimental conditions of milling case 2

ae (mm)	t (µm)	fz(mm/rev)	FX_mean (N)	FY_mean (N)	FZmedia (N)	FX_MAX (N)	FY_MAX (N)	FZ_MAX (N)	avg uncut chip thickness (µm)	Kt(N/mm^2)	Kr(N/mm^2)
0,1	30	0,03	10,98	17,26	4	75,5	76	30	0,0015	3588,878	11,8444842
0,1	30	0,04	15,93	27,08	6298	99,3	95,99	41,54	0,002	3469,66399	−58,8078643
0,1	30	0,05	19,43	34,71	7114	107,05	104,4	46,54	0,0025	3005,41943	−37,6654599
0,3	30	0,03	30,24	63,16	9	155,1	195,3	49,03	0,0025988	4841,51577	555,44787
0,3	30	0,04	39,97	75	12,48	169,2	211,9	57,17	0,0034641	3949,27581	442,492986
0,3	30	0,05	43,67	79,25	14,22	186,95	237,3	62,12	0,0043301	3517,14566	417,414929
0,5	30	0,03	49,15	101,8	14,76	194,75	293,25	66,36	0,0033541	5277,60357	1065,254
0,5	30	0,04	57,23	111,5	19	212,65	316,4	68,75	0,0044724	4291,16214	841,523622
0,5	30	0,05	73,32	119,6	22,03	245,15	337,95	82,85	0,0055901	3783,65243	602,165915
0,1	60	0,03	13,5	22,57	4,84	95,05	81,975	31,6	0,0015	4193,53965	−309,733263
0,1	60	0,04	17,63	27,68	5623	106,35	95,35	41,625	0,002	3583,54871	−195,43399
0,1	60	0,05	19,16	33,23	6	112,75	103,55	42,5	0,0025	3074,35433	−130,763106
0,3	60	0,03	27,55	62,66	7	147,25	184,15	50	0,0025980	4578,99065	509,851403
0,3	60	0,04	32,54	70,46	9,53	164,05	208,4	57,5	0,0034641	3859,6373	459,591661
0,3	60	0,05	44,29	79,96	13,85	181,1	229,25	60,75	0,0043301	3401,91095	399,176343
0,5	60	0,03	47,23	84,65	15,39	194,05	258,25	66,27	0,0033541	4891,51659	694,307682
0,5	60	0,04	57,13	97,67	18,7	215,05	286,2	73,83	0,0044721	4065,67437	577,102706
0,5	60	0,05	68,83	109,3	22,36	235,7	310,9	67,98	0,0055901	3546,80915	487,962035

Table 6
Data on the measured cutting forces and experimental conditions of milling case 3

ae(mm)	t(µm)	fz(mm/rev)	FY_mean(N)	FZmedia(N)	FX_MAX(N)	FY_MAX(N)	FZ_MAX(N)	avg uncut chip thickness (µm)	Kt(N/mm^2)	Kr(N/mm^2)
0,1	30	0,03	30,47	4,83	99,59	129,5	29,9	0,0015	5426,9057	708,537047
0,1	30	0,04	43,58	7	121	145,95	42	0,002	4742,8276	443,279823
0,1	30	0,05	50,04	7184	135,85	157,65	45,35	0,0025	4171,62735	309,851708
0,3	30	0,03	79,27	10,63	173,9	225,75	51,135	0,0025980	5522,00849	716,417216
0,3	30	0,04	82,64	12,63	182,05	243,3	55,175	0,0034641	4407,83119	634,723546
0,3	30	0,05	87,66	15,56	195,4	261,95	68,3	0,0043301	3791,55349	551,71725
0,5	30	0,03	107,6	9	202,15	312,05	70	0,0033541	5560,95032	1188,54228
0,5	30	0,04	115,9	12	226,85	327,2	93	0,0044721	4493,93892	813,945981
0,5	30	0,05	123,6	24,12	241,15	347,85	90,6	0,0055901	3821,93668	692,361025
0,1	60	0,03	37,48	5,85	110,2	117,4	26,8	0,0015	5391,60923	170,560573
0,1	60	0,04	44,08	7,1	119,15	126,15	38,05	0,002	4358,17798	124,367085
0,1	60	0,05	48,89	8656	129,5	138,35	48,63	0,0025	3807,05413	125,788423
0,3	60	0,03	80,35	11,58	180,65	224,9	55,27	0,0025980	5603,52945	611,407171
0,3	60	0,04	85,05	13,52	198	238,65	60	0,0034641	4524,93121	421,249178
0,3	60	0,05	92,07	15,6	212,25	254,5	69,375	0,0043301	3869,48199	350,263769
0,5	60	0,03	107,5	16,82	214,35	299,2	67,165	0,0033541	5553,92072	917,632506
0,5	60	0,04	117,8	20,27	232,3	333,55	79,355	0,0044721	4589,64956	821,245944
0,5	60	0,05	127,7	24,19	138,95	361,8	92,54	0,0055901	3249,29507	1446,04175

Table 7
Traditional produced Inconel 718 cutting force coefficients Vs Inconel 718 LPBF-ed cutting coefficients

| IN718 type	ae(mm)	Vc(m/min)	Fz(mm/rev)	Kt(N/mm^2)	Kr(N/mm^2)
Solution-treated and aged [87]	1.2	56.5	0.06	4372	
Solution-treated and aged [88]	1	60	0.07	4100	
wrought [89]	2.5	50	0.1	1042	302.8
wrought [90]	–	30	0.05	5800	
LPBF lt30(this research) Case 1	0.3	60	0.04	4726	1089
LPBF lt30 (this research) Case 2	0.3	60	0.04	3949	442
LPBF lt30 (this research) Case 3	0.3	60	0.04	4407	334
LPBF lt60(this research) Case 1	0.3	60	0.04	5090	901
LPBF lt60 (this research) Case 2	0.3	60	0.04	3859	459
LPBF lt60 (this research) Case 3	0.3	60	0.04	4524	421
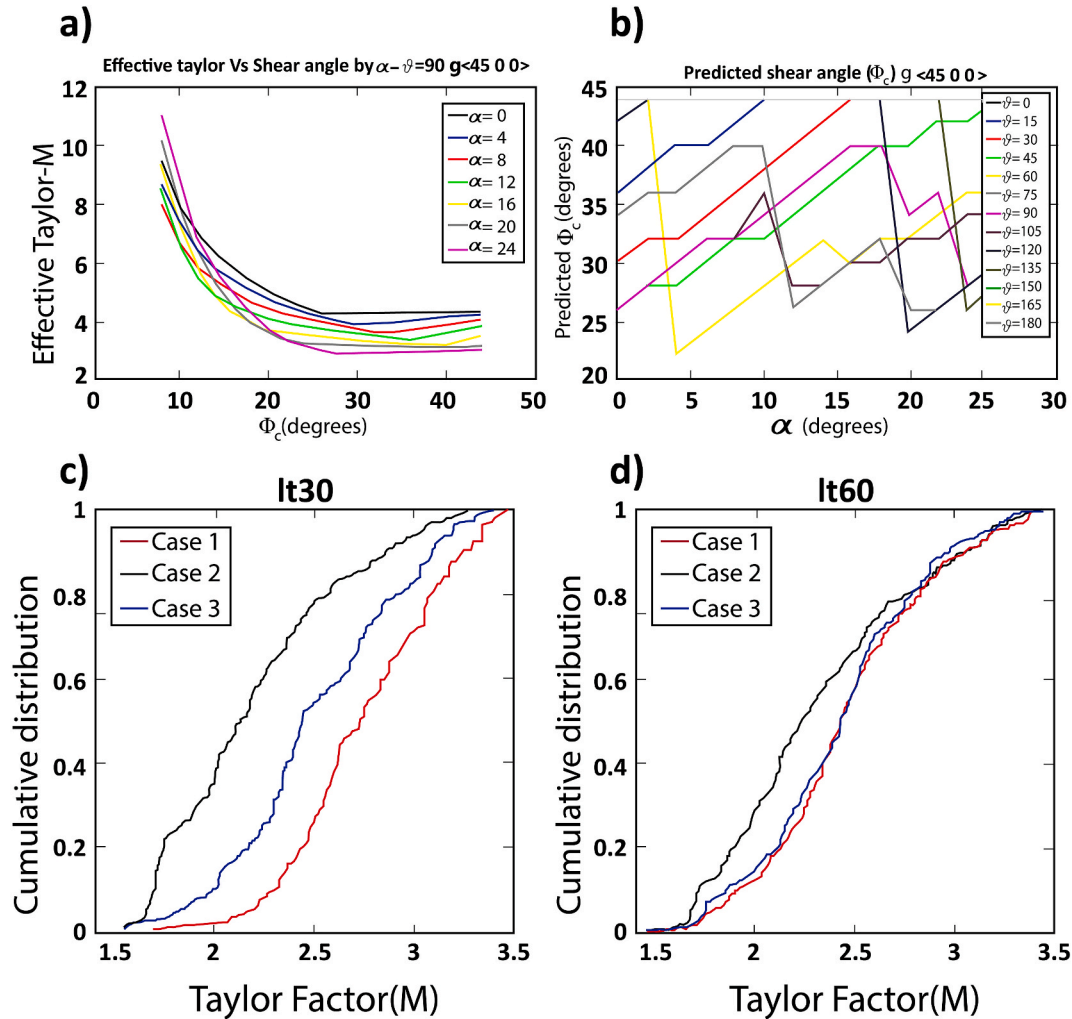
Fig. 26. a) Predicted shear angle by effective Taylor factor; b) Predicted shear angle by tool position and relative engagement angle; c), d) Comparison between the single crystal Taylor factor distributions for the lt30 and lt60 samples.

References

[1] J.M. Flynn, A. Shokrani, S.T. Newman, V. Dhokia, Hybrid additive and subtractive machine tools – research and industrial developments, Int. J. Mach. Tool Manufact. 101 (2016) 79–101, https://doi.org/10.1016/J.IJMACHTOOLS.2015.11.007.

[2] U.M. Dilberoglu, B. Gharehpapagh, U. Yaman, M. Dolen, The role of additive manufacturing in the Era of Industry 4.0, Procedia Manuf 11 (2017) 545–554, https://doi.org/10.1016/J.PROMFG.2017.07.148.

[3] M.K. Thompson, G. Moroni, T. Vaneker, G. Fadel, R.I. Campbell, I. Gibson, A. Bernard, J. Schulz, P. Graf, B. Ahuja, F. Martina, Design for additive manufacturing: trends, opportunities, considerations, and constraints, CIRP Ann 65 (2016) 737–760, https://doi.org/10.1016/J.CIRP.2016.05.004.

[4] A. la Monaca, J.W. Murray, Z. Liao, A. Speidel, J.A. Robles-Linares, D.A. Axinte, M. C. Hardy, A.T. Clare, Surface integrity in metal machining - Part II: functional performance, Int. J. Mach. Tool Manufact. 164 (2021) 103718, https://doi.org/10.1016/J.IJMACHTOOLS.2021.103718.

[5] G. Manogharan, Hybrid Manufacturing: Analysis of Integrating Additive and Subtractive Methods, 2014. https://repository.lib.ncsu.edu/handle/1840.16/9663. (Accessed 11 July 2021).

[6] N. Chen, P. Barnawal, M.C. Frank, Automated post machining process planning for a new hybrid manufacturing method of additive manufacturing and rapid machining, Rapid Prototyp. J. 24 (2018) 1077–1090, https://doi.org/10.1108/RPJ-04-2017-0057.

[7] S.Y. Liu, H.Q. Li, C.X. Qin, R. Zong, X.Y. Fang, The effect of energy density on texture and mechanical anisotropy in selective laser melted Inconel 718, Mater. Des. 191 (2020) 108642, https://doi.org/10.1016/j.matdes.2020.108642.

[8] N. Nadammal, S. Cabeza, T. Mishurova, T. Thiede, A. Kromm, C. Seyfert, L. Farahbod, C. Haberland, J.A. Schneider, P.D. Portella, G. Bruno, Effect of hatch length on the development of microstructure, texture and residual stresses in selective laser melted superalloy Inconel 718, Mater. Des. 134 (2017) 139–150, https://doi.org/10.1016/j.matdes.2017.08.049.

[9] D. Zhang, W. Niu, X. Cao, Z. Liu, Effect of standard heat treatment on the microstructure and mechanical properties of selective laser melting manufactured Inconel 718 superalloy, Mater. Sci. Eng. 644 (2015) 32–40, https://doi.org/10.1016/j.msea.2015.06.021.

[10] E. Chlebus, K. Gruber, B. Kuźnicka, J. Kurzac, T. Kurzynowski, Effect of heat treatment on the microstructure and mechanical properties of Inconel 718 processed by selective laser melting, Mater. Sci. Eng. 639 (2015) 647–655, https://doi.org/10.1016/j.msea.2015.05.035.

[11] E. Hosseini, V.A. Popovich, A review of mechanical properties of additively manufactured Inconel 718, Addit. Manuf. 30 (2019) 100877, https://doi.org/10.1016/j.addma.2019.100877.

[12] S. Sanchez, P. Smith, Z. Xu, G. Gaspard, C.J. Hyde, W.W. Wits, I.A. Ashcroft, H. Chen, A.T. Clare, Powder Bed Fusion of nickel-based superalloys: a review, Int. J. Mach. Tool Manufact. 165 (2021) 103729, https://doi.org/10.1016/J.IJMACHTOOLS.2021.103729.

[13] M. Xia, D. Gu, G. Yu, D. Dai, H. Chen, Q. Shi, Influence of hatch spacing on heat and mass transfer, thermodynamics and laser processability during additive manufacturing of Inconel 718 alloy, Int. J. Mach. Tool Manufact. 109 (2016) 147–157, https://doi.org/10.1016/J.IJMACHTOOLS.2016.07.010.

[14] L.E. Criales, Y.M. Arısoy, B. Lane, S. Moylan, A. Donmez, T. Özel, Laser powder bed fusion of nickel alloy 625: experimental investigations of effects of process parameters on melt pool size and shape with spatter analysis, Int. J. Mach. Tool Manufact. 121 (2017) 22–36, https://doi.org/10.1016/J.IJMACHTOOLS.2017.03.004.

[15] M. Ni, C. Chen, X. Wang, P. Wang, R. Li, X. Zhang, K. Zhou, Anisotropic tensile behavior of in situ precipitation strengthened Inconel 718 fabricated by additive manufacturing, Mater. Sci. Eng. 701 (2017) 344–351, https://doi.org/10.1016/j.msea.2017.06.098.

[16] Z. Chen, S. Chen, Z. Wei, L. Zhang, P. Wei, B. Lu, S. Zhang, Y. Xiang, Anisotropy of nickel-based superalloy K418 fabricated by selective laser melting, Prog. Nat. Sci. Mater. Int. 28 (2018) 496–504, https://doi.org/10.1016/j.pnsc.2018.07.001.

[17] Y. Yang, Y. Gong, S. Qu, Y. Rong, Y. Sun, M. Cai, Densification, surface morphology, microstructure and mechanical properties of 316L fabricated by hybrid manufacturing, Int. J. Adv. Manuf. Technol. 975 (97) (2018) 2687–2696, https://doi.org/10.1007/S00170-018-2144-1, 2018.

[18] D. Brown, C. Li, Z.Y. Liu, X.Y. Fang, Y.B. Guo, Surface integrity of Inconel 718 by hybrid selective laser melting and milling, Virtual Phys. Prototyp. 13 (2018) 26–31, https://doi.org/10.1080/17452759.2017.1392681.

[19] Y. Kok, X.P. Tan, P. Wang, M.L.S. Nai, N.H. Loh, E. Liu, S.B. Tor, Anisotropy and heterogeneity of microstructure and mechanical properties in metal additive manufacturing: a critical review, Mater. Des. 139 (2018) 565–586, https://doi.org/10.1016/J.MATDES.2017.11.021.

[20] C. Ni, L. Zhu, Z. Zheng, J. Zhang, Y. Yang, J. Yang, Y. Bai, C. Weng, W.F. Lu, H. Wang, Effect of material anisotropy on ultra-precision machining of Ti-6Al-4V alloy fabricated by selective laser melting, J. Alloys Compd. 848 (2020) 156457, https://doi.org/10.1016/j.jallcom.2020.156457.

[21] H.W. Yuchao Bai, Cuiling Zhao, Yu Zhang, Jie Chen, Additively manufactured CuCrZr alloy: microstructure, mechanical properties and machinability, Mater. Sci. Eng. 819 (2021).

[22] M. Sato, Y. Kato, K. Tsutiya, S. Aoki, Effects of crystal orientation on the cutting mechanism of aluminum single crystal, Bull. JSME. 24 (1981) 1864–1870, https://doi.org/10.1299/jsme1958.24.1864.

[23] M. Sato, Y. Kato, S. Aoki, A. Ikoma, Effects of crystal orientation on the cutting mechanism of the aluminum single Crystal : 2nd Report : on the (111) plane and the (112) end cutting, Bull. JSME. 26 (1983) 890–896, https://doi.org/10.1299/jsme1958.26.890.

[24] W.B. Lee, M. Zhou, A theoretical analysis of the effect of crystallographic orientation on chip formation in micromachining, Int. J. Mach. Tool Manufact. 33 (1993) 439–447, https://doi.org/10.1016/0890-6955(93)90050-5.

[25] W.B. Lee, S. To, Y.K. Sze, C.F. Cheung, Effect of material anisotropy on shear angle prediction in metal cutting - a mesoplasticity approach, in: Int. J. Mech. Sci., Pergamon, 2003, pp. 1739–1749, https://doi.org/10.1016/j.ijmecsci.2003.09.024.

[26] W.B. Lee, C.F. Cheung, S. To, A microplasticity analysis of micro-cutting force variation in ultra-precision diamond turning, J. Manuf. Sci. Eng. 124 (2002) 170–177, https://doi.org/10.1115/1.1454108.

[27] G.E. Bean, T.D. McLouth, D.B. Witkin, S.D. Sitzman, P.M. Adams, R.J. Zaldivar, Build orientation effects on texture and mechanical properties of selective laser melting inconel 718, J. Mater. Eng. Perform. 28 (2019) 1942–1949, https://doi.org/10.1007/s11665-019-03980-w.

[28] L. Thijs, M.L. Montero Sistiaga, R. Wauthle, Q. Xie, J.P. Kruth, J. Van Humbeeck, Strong morphological and crystallographic texture and resulting yield strength anisotropy in selective laser melted tantalum, Acta Mater. 61 (2013) 4657–4668, https://doi.org/10.1016/j.actamat.2013.04.036.

[29] P. Fernandez-Zelaia, V. Nguyen, H. Zhang, A. Kumar, S.N. Melkote, The effects of material anisotropy on secondary processing of additively manufactured CoCrMo, Addit. Manuf. 29 (2019) 100764, https://doi.org/10.1016/j.addma.2019.06.015.

[30] J. Fei, G. Liu, K. Patel, T. Özel, Cutting force investigation in face milling of additively fabricated nickel alloy 625 via powder bed fusion, Int. J. Mechatron. Manuf. Syst. 12 (2019) 196–210, https://doi.org/10.1504/IJMMS.2019.103484.

[31] danil yu pimenov, Hansong ji, Munish kumar gupta, quinghua song, wentong cai, tao zheng, youle zhao, zhanquian liu, Microstructure and machinability evaluation in micro milling of selective laser melted inconel 718 alloy, J. Mater. Res. Technol. (2021).

[32] M.S. Pham, B. Dovgyy, P.A. Hooper, C.M. Gourlay, A. Piglione, The role of side-branching in microstructure development in laser powder-bed fusion, Nat. Commun. 11 (2020) 1–12, https://doi.org/10.1038/s41467-020-14453-3.

[33] J. Liu, A.C. To, Quantitative texture prediction of epitaxial columnar grains in additive manufacturing using selective laser melting, Addit. Manuf. 16 (2017) 58–64, https://doi.org/10.1016/j.addma.2017.05.005.

[34] A. Basak, S. Das, Epitaxy and microstructure evolution in metal additive manufacturing, Annu. Rev. Mater. Res. 46 (2016) 125–149, https://doi.org/10.1146/annurev-matsci-070115-031728.

[35] L.L. Parimi, G. Ravi, D. Clark, M.M. Attallah, Microstructural and texture development in direct laser fabricated IN718, Mater. Char. 89 (2014) 102–111, https://doi.org/10.1016/j.matchar.2013.12.012.

[36] K. Moussaoui, W. Rubio, M. Mousseigne, T. Sultan, F. Rezai, Effects of Selective Laser Melting additive manufacturing parameters of Inconel 718 on porosity, microstructure and mechanical properties, Mater. Sci. Eng. 735 (2018) 182–190, https://doi.org/10.1016/j.msea.2018.08.037.

[37] Z. Liu, H. Qi, Effects of substrate crystallographic orientations on crystal growth and microstructure formation in laser powder deposition of nickel-based superalloy, Acta Mater. 87 (2015) 248–258, https://doi.org/10.1016/j.actamat.2014.12.046.

[38] G.P. Dinda, A.K. Dasgupta, J. Mazumder, Texture control during laser deposition of nickel-based superalloy, Scripta Mater. 67 (2012) 503–506, https://doi.org/10.1016/j.scriptamat.2012.06.014.

[39] H.L. Wei, T. Mukherjee, T. DebRoy, Grain growth modeling for additive manufacturing of nickel based superalloys, in: Proc. 6th Int. Conf. Recrystal. Grain Growth, ReX GG 2016, Springer International Publishing AG, 2016, pp. 265–269, https://doi.org/10.1007/978-3-319-48770-0_39.

[40] G.E. Bean, T.D. McLouth, D.B. Witkin, S.D. Sitzman, P.M. Adams, R.J. Zaldivar, Build orientation effects on texture and mechanical properties of selective laser melting inconel 718, J. Mater. Eng. Perform. 28 (2019) 1942–1949, https://doi.org/10.1007/s11665-019-03980-w.

[41] M. Gäumann, S. Henry, F. Cléton, J.D. Wagnière, W. Kurz, Epitaxial laser metal forming: analysis of microstructure formation, Mater. Sci. Eng. 271 (1999) 232–241, https://doi.org/10.1016/s0921-5093(99)00202-6.

[42] W. Kurz, C. Bezençon, M. Gäumann, Columnar to equiaxed transition in solidification processing, Sci. Technol. Adv. Mater. 2 (2001) 185–191, https://doi.org/10.1016/S1468-6996(01)00047-X.

[43] M. Rappaz, S.A. David, J.M. Vitek, L.A. Boatner, Development of microstructures in Fe-15Ni-15Cr single crystal electron beam welds, Metall. Trans. A. 20 (1989) 1125–1138, https://doi.org/10.1007/BF02650147.

[44] H.L. Wei, J. Mazumder, T. DebRoy, Evolution of solidification texture during additive manufacturing, Sci. Rep. 5 (2015) 1–7, https://doi.org/10.1038/srep16446.

[45] H.Y. Wan, Z.J. Zhou, C.P. Li, G.F. Chen, G.P. Zhang, Effect of scanning strategy on grain structure and crystallographic texture of Inconel 718 processed by selective laser melting, J. Mater. Sci. Technol. 34 (2018) 1799–1804, https://doi.org/10.1016/j.jmst.2018.02.002.

[46] M. Higashi, T. Ozaki, Selective laser melting of pure molybdenum: evolution of defect and crystallographic texture with process parameters, Mater. Des. 191 (2020), https://doi.org/10.1016/j.matdes.2020.108588.

[47] Y. Wang, J. Shi, Y. Liu, Competitive grain growth and dendrite morphology evolution in selective laser melting of Inconel 718 superalloy, J. Cryst. Growth 521 (2019) 15–29, https://doi.org/10.1016/j.jcrysgro.2019.05.027.

[48] S.H. Sun, K. Hagihara, T. Nakano, Effect of scanning strategy on texture formation in Ni-25 at.%Mo alloys fabricated by selective laser melting, Mater. Des. 140 (2018) 307–316, https://doi.org/10.1016/j.matdes.2017.11.060.

[49] M.S. Pham, B. Dovgyy, P.A. Hooper, C.M. Gourlay, A. Piglione, The role of side-branching in microstructure development in laser powder-bed fusion, Nat. Commun. 11 (2020) 1–12, https://doi.org/10.1038/s41467-020-14453-3.

[50] C. Moussa, M. Bernacki, R. Besnard, N. Bozzolo, Statistical analysis of dislocations and dislocation boundaries from EBSD data, Ultramicroscopy 179 (2017) 63–72, https://doi.org/10.1016/j.ultramic.2017.04.005.

[51] H.L. Wei, J.W. Elmer, T. Debroy, Origin of grain orientation during solidification of an aluminum alloy, Acta Mater. 115 (2016) 123–131, https://doi.org/10.1016/j.actamat.2016.05.057.

[52] H. Gong, K. Rafi, H. Gu, T. Starr, B. Stucker, Analysis of defect generation in Ti-6Al-4V parts made using powder bed fusion additive manufacturing processes, Addit. Manuf. 1 (2014) 87–98, https://doi.org/10.1016/j.addma.2014.08.002.

[53] L. Thijs, F. Verhaeghe, T. Craeghs, J. Van Humbeeck, J.P. Kruth, A study of the microstructural evolution during selective laser melting of Ti-6Al-4V, Acta Mater. 58 (2010) 3303–3312, https://doi.org/10.1016/j.actamat.2010.02.004.

[54] T. DebRoy, H.L. Wei, J.S. Zuback, T. Mukherjee, J.W. Elmer, J.O. Milewski, A.M. Beese, A. Wilson-Heid, A. De, W. Zhang, Additive manufacturing of metallic components – process, structure and properties, Prog. Mater. Sci. 92 (2018) 112–224, https://doi.org/10.1016/j.pmatsci.2017.10.001.

[55] N. C.c, S. M.M, L. M.L, H.C. Man, Microstructure and mechanical properties of selective laser melted magnesium, Appl. Surf. Sci. 257 (2011) 7447–7454, https://doi.org/10.11896/cldb.19040019.

[56] J.H. Yi, J.W. Kang, T.J. Wang, X. Wang, Y.Y. Hu, T. Feng, Y.L. Feng, P.Y. Wu, Effect of laser energy density on the microstructure, mechanical properties, and deformation of Inconel 718 samples fabricated by selective laser melting, J. Alloys Compd. 786 (2019) 481–488, https://doi.org/10.1016/j.jallcom.2019.01.377.

[57] Z. Lei, J. Bi, Y. Chen, X. Chen, X. Qin, Z. Tian, Effect of energy density on formability, microstructure and micro-hardness of selective laser melted Sc- and Zr- modified 7075 aluminum alloy, Powder Technol. 356 (2019) 594–606, https://doi.org/10.1016/j.powtec.2019.08.082.

[58] L.E. Criales, Y.M. Arısoy, B. Lane, S. Moylan, A. Donmez, T. Özel, Laser powder bed fusion of nickel alloy 625: experimental investigations of effects of process parameters on melt pool size and shape with spatter analysis, Int. J. Mach. Tool Manufact. 121 (2017) 22–36, https://doi.org/10.1016/j.ijmachtools.2017.03.004.

[59] J.J.S. Dilip, S. Zhang, C. Teng, K. Zeng, C. Robinson, D. Pal, B. Stucker, Influence of processing parameters on the evolution of melt pool, porosity, and microstructures in Ti-6Al-4V alloy parts fabricated by selective laser melting, Prog. Addit. Manuf. 2 (2017) 157–167, https://doi.org/10.1007/s40964-017-0030-2.

[60] U. Scipioni Bertoli, A.J. Wolfer, M.J. Matthews, J.P.R. Delplanque, J.M. Schoenung, On the limitations of volumetric energy density as a design parameter for selective laser melting, Mater. Des. 113 (2017) 331–340, https://doi.org/10.1016/j.matdes.2016.10.037.

[61] K.H. Lee, G.J. Yun, A novel heat source model for analysis of melt Pool evolution in selective laser melting process, Addit. Manuf. 36 (2020) 101497, https://doi.org/10.1016/j.addma.2020.101497.

[62] M.A. Easton, D.H. StJohn, Improved prediction of the grain size of aluminum alloys that includes the effect of cooling rate, Mater. Sci. Eng. 486 (2008) 8–13, https://doi.org/10.1016/j.msea.2007.11.009.

[63] M.Y. Mendoza, P. Samimi, D.A. Brice, I. Ghamarian, M. Rolchigo, R. LeSar, P.C. Collins, On the role of composition and processing parameters on the microstructure evolution of Ti-xMo alloys, BMC Chem 13 (2019) 1–8, https://doi.org/10.1186/s13065-019-0529-3.

[64] J. Dai, M.A. Easton, M. Zhang, D. Qiu, X. Xiong, W. Liu, G. Wu, Effects of cooling rate and solute content on the grain refinement of Mg-Gd-Y alloys by aluminum, Metall. Mater. Trans. A Phys. Metall. Mater. Sci. 45 (2014) 4665–4678, https://doi.org/10.1007/s11661-014-2390-2.

[65] M. Ma, Z. Wang, X. Zeng, A comparison on metallurgical behaviors of 316L stainless steel by selective laser melting and laser cladding deposition, Mater. Sci. Eng. 685 (2017) 265–273, https://doi.org/10.1016/j.msea.2016.12.112.

[66] T. Komatsu, T. Yoshino, T. Matsumura, S. Torizuka, Effect of crystal grain size in stainless steel on cutting process in micromilling, Procedia CIRP 1 (2012) 150–155, https://doi.org/10.1016/j.procir.2012.04.026.

[67] M.Z. xian Wu, li Liang, Chengjiao Yao, Influence of the cutting edge radius and the material grain size on the cutting force in micro cutting, Precis. Eng. 45 (2016) 359–364.

[68] F.J. Zerilli, R.W. Armstrong, Dislocation-mechanics-based constitutive relations for material dynamics calculations, J. Appl. Phys. 61 (1987) 1816–1825, https://doi.org/10.1063/1.338024.

[69] F.J. Zerilli, R.W. Armstrong, Constitutive relations for the plastic deformation of metals, in: AIP Conf. Proc., AIP Publishing, 2008, pp. 989–992, https://doi.org/10.1063/1.46201.

[70] R. C.N, Deformation Geometry for Materials Scientists, Elsevier, 1973, https://doi.org/10.1016/C2013-0-02546-7.

[71] C. Przybyla, Methodology for Determining the Variance of the Taylor Factor: Application in Fe-3%Si, 2005. https://scholarsarchive.byu.edu/etd/687. (Accessed 12 July 2021).

[72] J.-H. Cho, A.D. Rollett, K.H. Oh, Determination of volume fractions of texture components with standard distributions in euler space, Metall. Mater. Trans. 35 (2004) 1075–1086, https://doi.org/10.1007/s11661-004-0033-8.

[73] A. Leicht, C.H. Yu, V. Luzin, U. Klement, E. Hryha, Effect of scan rotation on the microstructure development and mechanical properties of 316L parts produced by laser powder bed fusion, Mater. Char. 163 (2020) 110309, https://doi.org/10.1016/j.matchar.2020.110309.

[74] F. Geiger, K. Kunze, T. Etter, Tailoring the texture of IN738LC processed by selective laser melting (SLM) by specific scanning strategies, Mater. Sci. Eng. 661 (2016) 240–246, https://doi.org/10.1016/j.msea.2016.03.036.

[75] N. Nadammal, S. Cabeza, T. Mishurova, T. Thiede, A. Kromm, C. Seyfert, L. Farahbod, C. Haberland, J.A. Schneider, P.D. Portella, G. Bruno, Effect of hatch length on the development of microstructure, texture and residual stresses in selective laser melted superalloy Inconel 718, Mater. Des. 134 (2017) 139–150, https://doi.org/10.1016/j.matdes.2017.08.049.

[76] L. Thijs, K. Kempen, J.P. Kruth, J. Van Humbeeck, Fine-structured aluminium products with controllable texture by selective laser melting of pre-alloyed AlSi10Mg powder, Acta Mater. 61 (2013) 1809–1819, https://doi.org/10.1016/j.actamat.2012.11.052.

[77] D. Wang, C. Yu, J. Ma, W. Liu, Z. Shen, Densification and crack suppression in selective laser melting of pure molybdenum, Mater. Des. 129 (2017) 44–52, https://doi.org/10.1016/j.matdes.2017.04.094.

[78] Y. Ji, L. Chen, L.Q. Chen, Understanding microstructure evolution during additive manufacturing of metallic alloys using phase-field modeling, thermo-mechanical model, Addit. Manuf. (2018) 93–116, https://doi.org/10.1016/B978-0-12-811820-7.00008-2.

[79] M.W. Fu, J.L. Wang, Size effects in multi-scale materials processing and manufacturing, Int. J. Mach. Tool Manufact. 167 (2021) 103755, https://doi.org/10.1016/J.IJMACHTOOLS.2021.103755.

[80] N. Chen, H.N. Li, J. Wu, Z. Li, L. Li, G. Liu, N. He, Advances in micro milling: from tool fabrication to process outcomes, Int. J. Mach. Tool Manufact. 160 (2021) 103670, https://doi.org/10.1016/J.IJMACHTOOLS.2020.103670.

[81] A. Mouritz, Strengthening of metal alloys, in: Introd. To Aerosp. Mater., Woodhead Publishing, 2012, pp. 57–90, https://doi.org/10.1533/9780857095152.57.

[82] J. Polák, Cyclic deformation, crack initiation, and low-cycle fatigue, in: Ref. Modul. Mater. Sci. Mater. Eng., Elsevier, 2016, https://doi.org/10.1016/B978-0-12-803581-8.00890-0.

[83] A. Godon, J. Creus, S. Cohendoz, E. Conforto, X. Feaugas, P. Girault, C. Savall, Effects of grain orientation on the Hall-Petch relationship in electrodeposited nickel with nanocrystalline grains, Scripta Mater. 62 (2010) 403–406, https://doi.org/10.1016/j.scriptamat.2009.11.038.

[84] E.G. Dere, H. Sharma, R.H. Petrov, J. Sietsma, S.E. Offerman, Effect of niobium and grain boundary density on the fire resistance of Fe–C–Mn steel, Scripta Mater. 68 (2013) 651–654, https://doi.org/10.1016/J.SCRIPTAMAT.2012.12.030.

[85] M. Papanikolaou, K. Salonitis, Grain size effects on nanocutting behaviour modelling based on molecular dynamics simulations, Appl. Surf. Sci. 540 (2021) 148291, https://doi.org/10.1016/J.APSUSC.2020.148291.

[86] T.G. Nieh, L.M. Hsiung, J. Wadsworth, R. Kaibyshev, High strain rate superplasticity in a continuously recrystallized Al–6%Mg–0.3%Sc alloy, Acta Mater. 46 (1998) 2789–2800, https://doi.org/10.1016/S1359-6454(97)00452-7.

[87] C.-J. Lin, Y.-T. Lui, Y.-F. Lin, H.-B. Wang, S.Y. Liang, J.-J.J. Wang, Prediction of shearing and ploughing constants in milling of inconel 718, J. Manuf. Mater. Process. 5 (5) (2021) 8, https://doi.org/10.3390/JMMP5010008 (2021) 8.

[88] A. Moufki, G. Le Coz, D. Dudzinski, End-milling of inconel 718 superalloy-an analytical modelling, in: Procedia CIRP, Elsevier B.V., 2017, pp. 358–363, https://doi.org/10.1016/j.procir.2017.03.330.

[89] Z. Zhang, Z. Liang, M. Luo, B. Wu, D. Zhang, A general method for calibration of milling force coefficients and cutter runout parameters simultaneously for helical end milling, Int. J. Adv. Manuf. Technol. 2021 (2021) 1–9, https://doi.org/10.1007/S00170-021-07657-4.

[90] J.-C. Tsai, C.-Y. Kuo, Z.-P. Liu, K.H.-H. Hsiao, An investigation on the cutting force of milling Inconel 718, MATEC Web Conf 169 (2018) 01039, https://doi.org/10.1051/MATECCONF/201816901039.